Morphology- and Crystal Packing-Dependent Singlet Fission and Photodegradation in Functionalized Tetracene Crystals and Films

Winston T. Goldthwaite,[1] Evan Lambertson,[1] Madalyn Gragg,[1] Dean Windemuller,[3] John E. Anthony,[3] Tim Zuehlsdorff,[2] and Oksana Ostroverkhova[1]*

[1] Department of Physics, Oregon State University, Corvallis, OR 97331

[2] Department of Chemistry, Oregon State University, Corvallis, OR 97331

[3] Department of Chemistry, University of Kentucky, Lexington, KY 40511

*oksana@science.oregonstate.edu

October 17, 2024

Abstract

Singlet fission (SF) is a charge carrier multiplication process that has potential for improving the performance of (opto)electronic devices from the conversion of one singlet exciton S1 into two triplet excitons T1 via a spin-entangled triplet pair state ^{1}(TT). This process depends highly on molecular packing and morphology, both for the generation and dissociation of ^{1}(TT) states. Many benchmark SF materials such as acenes are also prone to photodegradation reactions, such as endoperoxide (EPO) formation and photodimerization, which inhibit realization of SF devices. In this paper, we compare functionalized tetracenes R-Tc with two packing motifs: 'slip-stack' packing in R = TES, TMS, and tBu, and 'gamma' packing in R = TBDMS to determine the effects of morphology on SF, as well as on photodegradation using a combination of temperature and magnetic field dependent spectroscopy, kinetic modeling, and time-dependent density functional theory (TDDFT). We find that both 'slip-stack' and 'gamma' packing support SF with high T1 yield at room temperature (up to 191% and 181%, respectively), but 'slip-stack' is considerably more advantageous at low tempera-

tures (<150 K). Additionally, each packing structure has a distinct emissive relaxation pathway competitive to SF, while the states involved in the SF itself are dark. The 'gamma' packing has superior photostability, both in regards to EPO formation and photodimerization. The results indicate that the tradeoff between SF efficiency and photostability can be overcome with material design, emphasize the importance of considering both photophysical and photochemical properties, and inform efforts to develop optimal SF materials for (opto)electronic applications.

1 Introduction

With the urgent need for development of efficient clean energy solutions and energy-efficient electronics, a major goal in semiconductor research is to enhance efficiency of (opto)electronic devices such as solar cells. Towards that goal, one promising process is singlet fission (SF), a carrier multiplication process that involves spin-allowed conversion of one singlet exciton (S1) into two triplet excitons (T1 + T1) that produce two pairs of charge carriers. SF photovoltaic devices can potentially break the Shockley-Queisser energy conversion limit in silicon,[1,2] and in the past decade there has been significant research on many SF systems which meet the basic SF energy requirement, where the energy of the singlet state E(S1) is comparable to double of the energy of the triplet state, 2E(T1).[3] Acenes are benchmark SF materials and model systems for understanding physical mechanisms, with pentacene (Pn) and hexacene exhibiting exothermic SF (E(S1)>2E(T1)) and tetracene (Tc) the endothermic SF (E(S1)<2E(T1)).[4–6] Functionalized acenes such as R-Pn and R-Tc (e.g., Fig. 1a) enable solution processability and control over the molecular packing motifs by varying the side group R. Tetracene derivatives are of special interest because of their favorable energetics for conjugation with c-Si solar cells.[7,8] SF in functionalized Tc derivative TIPS-Tc has been extensively studied,[9–13] with conflicting results regarding the nature, properties, and role in the SF of entangled triplet pairs ^{1}(TT), excimers, and other excited states. Here, we present a comprehensive study of novel R-Tc derivatives to clarify the physical picture and resolve some of the issues raised in previous studies.

The singlet fission process proceeds upon photoexcitation of a molecule in its excited singlet state (S1), after which the excitation is redistributed between the excited molecule and the neighboring molecule in the ground state (S0) to create an entangled triplet pair ^{1}(TT), which then gradually loses entanglement and becomes spin-mixed as the triplets separate into ^{l}(T...T) (l = 1,3,5) and further into free triplets T1: (S0 + S1) → ^{1}(TT) → ^{l}(T...T) → (T1 + T1).[3] The spin-correlated triplet pair state ^{1}(TT) is an important intermediate step

which can be thought of as two entangled triplet states occupying neighboring molecules. This ^{1}(TT) state can be formed through vibronic coupling to S1, through an intermediate charge transfer state, or from the reverse to SF process of triplet-triplet annihilation (TTA),[3] but the formation and dissociation of ^{1}(TT) is dependent on the molecular packing and morphology. To better understand what morphologies are conducive to ^{1}(TT) formation and dissociation, as well as to the formation of unproductive states which may compete with the SF, we study R-Tc derivatives with two distinct packing motifs: 'slip-stack' (TES-, TMS-, tBu-Tc) and 'gamma' (TBDMS-Tc), with the three 'slip-stacked' derivatives exhibiting slightly different intermolecular orientations. The side groups R have only a minor effect on the optical properties of isolated (non-interacting) molecules (e.g., in dilute solutions),[14,15] but a significant effect on the morphology of R-Tc aggregates in the solid state, causing large differences in photophysical and photochemical behavior that can be directly related to molecular packing.

One of the main obstacles to the practical application of acenes in (opto)electronic devices, including SF photovoltaics, is their photodegradation.[1] Photodegradation of acenes in the presence of oxygen has been studied both in solutions[16–18] and in the solid state.[19–22] However, establishing the relationship between the SF properties and photodegradation is at its inception, and it is necessary for the development of singlet fission-based (opto)electronic devices.[18, 20, 23]

There are two main degradation processes of note: endoperoxide (EPO) formation, where an oxygen molecule bonds to the acene core;[16,18] and dimerization, where two neighboring acene molecules bond together.[20,24] In both cases, the degraded molecules no longer have the desired (opto)electronic properties, including SF. The prevention or reversal of these photodegradation processes thus have been an important area of study.[16,18,20] While photodegradation is a hindrance for high-performance organic devices, it can also be used as a tool for understanding the photophysical processes of interest like SF.[23] Additionally, some of the photodegradation processes such as EPO formation which relies on the generation of reactive oxygen species - singlet oxygen ($^1O_2$) and superoxide (O_2^-) - can be of interest for applications in photocatalysis and photodynamic therapy,[25,26] whereas photodimerization can be of interest for optomechanical applications.[27] Therefore, understanding of how SF properties are intertwined with processes responsible for photostability is important for applications relying both on the stability of devices and on the ability to undergo chemical reactions, which motivates our side-by-side study of photophysical and photochemical properties.

In particular, in this paper we seek to address the following questions: (i) How does morphology affect SF and the properties of states competitive to SF? (ii) How does morphology affect the photostability in aerobic and anaerobic environments? (iii) How do the excited states dynamics affect photostability, and is it possible to achieve both high singlet fission yields and photostability?

We studied films and crystals of R-Tc (R= TES, TBDMS, TMS, and tBu) derivatives and applied a combination of steady-state and time-resolved spectroscopy in the 1.6-300 K temperature range at 0-7 T magnetic fields, kinetic modeling, and the time-dependent density functional theory (TDDFT). In R-Tc crystals, we reveal the presence of temperature-independent and temperature-dependent SF pathways, with pronounced morphology dependence of the SF at <150 K, and of competitive to SF states with morphology-dependent properties. Although large differences in photostability were observed depending on morphology, our data suggests that it is possible to combine an efficient SF with enhanced photostability.

2 Materials and Methods

2.1 Materials

Molecular structures of the tetracene derivatives (R-Tc) functionalized with side groups R = TES [(triethylsilyl)ethynyl], TBDMS [(tert-butyldimethylsilyl)ethynyl], TMS [(trimethylsilyl)ethynyl], and tBu [tertbutylethynyl] used in our studies are shown in Fig. 1a. Synthesis is described in the Supplementary Material (Sec. S1). TES-Tc and TBDMS-Tc represent the most distinct cases in terms of molecular packing ('slip-stack' and 'gamma' respectively, Figs. 1b-c) and as such are the main focus in this paper. The 'gamma' packing in TBDMS-Tc is similar to 'herringbone' packing, but consists of an infinite stack (face-to-face) along one axis, and a herringbone arrangement along another axis (Fig. S5a).[28] The packing motifs of TMS-Tc and tBu-Tc are similar to that of TES-Tc, but with closer molecular arrangements afforded by smaller volumes of the TMS and tBu side groups as compared to TES,[23] and so these derivatives are used to fine-tune our understanding of packing and morphology effects on photophysics and photochemistry under study and to establish the generality of our conclusions.

The TES-Tc single crystal has a triclinic structure with two molecules per unit cell ($Z = 2$) and unit cell parameters a = 11.83 Å, b = 12.38 Å, c = 13.2 Å, $\alpha = 64.02^\circ$, $\beta = 72.39^\circ$, and $\gamma = 63.99^\circ$. The TBDMS-Tc single crystal has a monoclinic structure with four molecules

per unit cell ($Z = 4$) and unit cell parameters a = 6.90 Å, b = 32.67 Å, c = 13.32 Å, $\alpha = 90.0^{\circ}$, $\beta = 98.22^{\circ}$, and $\gamma = 90.0^{\circ}$. X-ray diffraction data from solution-grown R-Tc crystals on glass/Ag substrates are shown in Fig. S4, with $(0l\,0)$ ($l = 2,6$) and (100) as predominant orientations for TBDMS-Tc and TES-Tc, respectively. The structures of the TMS-Tc and tBu-Tc crystals are described in the Supplementary Material (Sec. S2).

2.2 Sample preparation

Both single crystal and two types of R-Tc thin films ('blended' films of R-Tc:PMMA, PMMA = polymethylmethacrylate, and 'pristine' films of only R-Tc) were fabricated. In blended films (in which the R-Tc molecules are dispersed in a PMMA polymer matrix), the relative concentrations of R-Tc and PMMA were varied to achieve the average intermolecular spacing of R-Tc molecules (d) of either d = 2 nm or d = 1 nm.[29] The R-Tc molecules in d = 2 nm films, on average, are fairly isolated from each other, and behave more similarly to those in a dilute solution. In d = 1 nm films, groups of molecules form aggregates within the PMMA and exhibit significant intermolecular interactions, undergoing SF and photodimerization. Pristine films are the most aggregated and have large differences in morphology between R-Tc derivatives. For example, TES-Tc forms homogeneous amorphous films, while TBDMS-Tc favors forming polycrystalline films with larger spot-to-spot variation.

Films were fabricated by spincasting solutions onto a glass substrate coated with a 50 nm Ag mirror; these will be referred to as 'bottom' mirror samples where the film is exposed to oxygen. Some samples were spincast onto glass, then capped with 50 nm Ag deposited via thermal evaporation to make 'top' mirror films, which are protected from oxygen. Pristine films were made from 50 mM R-Tc solutions in toluene by spincasting at 2000-3000 RPM. Blended films used 0.3 M PMMA in toluene with a concentration of R-Tc to yield the desired average intermolecular spacing d as described in Ref.[29]

Single crystals were grown from 3-5 mM R-Tc chlorobenzene solutions dropcast onto a 50 nm Ag coated glass substrate. The sample was left in a 0 °C chiller to slow the evaporation of the solvent and leave behind multiple crystals. The quality of crystals formed throughout a sample varied, and high quality single crystals were identified for further study using polarization microscopy. In all derivatives, crystals were needle-like, with up to 1 mm length and ~5-20 μm width. The optical density (OD) of crystals under study varied between 0.4-0.7 at the absorption maximum, where TBDMS-Tc crystals typically have lower OD than TES-Tc, and the effects of self-absorption on emissive properties were found to be relatively minor (Fig. S17).

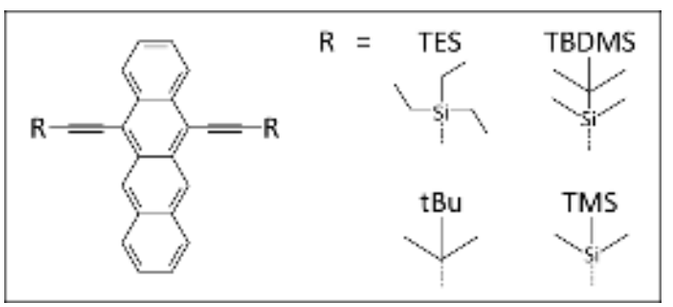

(a)

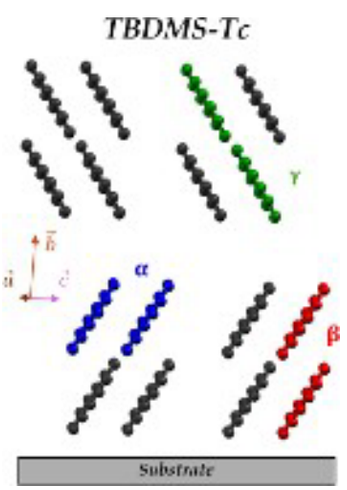

(b)

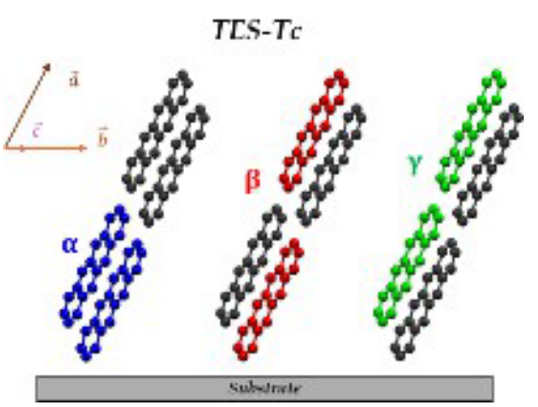

(c)

Figure 1: a) R-Tetracene molecular structure and side groups R = TES, TBDMS, tBu, and TMS. b) TBDMS-Tc 'gamma' crystal packing (020) relative to the substrate, and c) TES-Tc 'slip-stack' packing (100) relative to the substrate.

2.3 Measurements of optical properties

Steady-state optical absorption measurements were taken using white light from a tungsten filament lamp (Fiber-Lite DC-950) and spectra were collected through either a fiber-coupled Ocean Optics USB2000 spectrometer or a PI SpectraPro HRS 300 spectrometer. Absorption was measured in solutions using transmissive geometry, and in films and crystals using reflective geometry, as described in our previous publications.[15,29] Steady-state photoluminescence (PL) measurements were taken using a 532 nm continuous wave (cw) laser (Verdi-5, Coherent, Inc.) excitation with 5 μW power ($\sim$20 W/cm^2) and spectra were collected with a PI SpectraPro HRS 300 spectrometer. Selected PL data were taken using 633 nm cw excitation (HeNe laser) and 639 nm (NOPA, Orpheus-N, Light Conversion). Absorption and PL measurements on films and crystals were performed in a microscope, with a 10x 0.28 NA objective and the illumination spot size of below $\sim$5 μm.

The lifetimes of emissive excited states (PL lifetimes) were measured using time-correlated single photon counting (TCSPC) with a Picoquant TimeHarp 260 and a MPD PDM single photon detector with the instrument response function (IRF) of about 200 ps. A 100-fs, 200 kHz pulsed 515 nm excitation with $\sim$3 μW power ($\sim$0.15 mJ/cm^2) was generated by frequency-doubling of a 1030 nm laser (Pharos, Light Conversion). PL lifetimes were spectrally filtered into different emissive bands to determine the decay rates of various states.

The dependence of PL spectra and lifetimes on external magnetic fields (B-fields) and temperature was obtained by placing samples in a magneto-optical cryostat (OptiCool, Quantum Design) with a temperature range of 1.6-300 K and a B-field range of 0-7 T with orientation perpendicular to the substrate.

To study photodegradation of films and crystals, samples were continually exposed to 532 nm cw laser (for PL-based measurements) or to white light (for absorption-based measurements) excitation, as described in our previous work.[20,23] Absorption or PL spectra were taken at periodic intervals to track changes in the spectra over time caused by the photodegradation. 'Bottom' samples were used for measurements in air, whereas 'top' samples or any samples placed in the cryostat under vacuum were used for measurements in an anaerobic environment. Selected experiments were performed as a function of temperature and B-field. The excitation intensities were $\sim$40 W/cm^2 for the 532 nm laser and $\sim$50 W/cm^2 for the white light, although only $\sim$20 W/cm^2 of the white light is in the wavelength range absorbed by the crystals.

2.4 Computational Methods

Details on DFT and TDDFT calculations can be found in the Supplementary Material Sec. S7. All calculations were carried out with the Gaussian 16 software package.[30] Energies and oscillator strength estimates for singlet excited state transitions were calculated using TDDFT at the CAM-B3LYP/6-31+G* level of theory.[31,32] Both the difference in self-consistent field energies between ground state configurations (ΔSCF) and TDDFT in both unoptimized and optimized geometries were used to estimate triplet state energies in R-Tc monomers.

To compare the extent of intermolecular interactions present in each packing geometry, non-covalent dimers with notable π-π overlap within the R-Tc crystal structures were isolated, and the energy splittings were used to estimate the magnitudes of nearest-neighbor transfer and hopping integrals (t_e and t_h) as well as resonant intermolecular couplings (V).[15] The four lowest-lying singlet excited states in each dimer pair were identified through TDDFT and excitonic character was assigned through natural transition orbitals (NTOs), as described in previous work.[15]

3 Results

3.1 Optical properties of solutions

The absorption spectra of R-Tc (R= TES, TBDMS, TMS) in dilute (<20 μM) toluene solution are identical (Fig. S8a), which indicates that the side groups have a minor influence on the optical properties of the isolated molecules, similar to previously studied anthradithophene (ADT) and Pn derivatives.[14,15,33] In all solutions, the absorption spectra are well described by a Frank–Condon (FC) vibronic progression (Eq. S1) with the homogeneously broadened 0-0 resonance at 2.32 eV (or 533 nm) in TES-, TMS-, and TBDMS-Tc derivatives with FWHM = 0.051-0.057 eV, followed by 0-n (n = 1, 2, 3) vibronic replica peaks at 0.17 eV intervals due to the exciton coupling to a C=C/C–C stretch modes of the R-Tc backbone with the Huang–Rhys factors of ~0.84-0.98 (Figs. 2a and S8). Fit parameters are summarized in Table S1. The spectra of tBu-Tc solutions are ~8 nm (~0.03 eV) blue-shifted from those of other R-Tc derivatives. This is supported by the TDDFT calculations (Table S12) predicting ~0.04-0.05 eV blue shift due to the absence of the Si atom on the tBu side groups as compared to TES, TMS, and TBDMS (Fig. 1a).

All derivatives exhibited PL (Figs. 2b-c and S8b) with a small ≤7 nm Stokes shift,

similar to other functionalized acenes and acenethiophenes,[15,29] with the 0-0 emission peak at 2.29 eV, or 540 nm (2.32 eV, or 533 nm) and FWHM = 0.09 eV in TES-Tc, TMS-, and TBDMS-Tc (tBu-Tc), followed by vibronic replica peaks with an energy spacing of ~0.16 eV. Fit parameters can be found in Table S2. The time-resolved PL exhibited monoexponential decay (Fig. 2d) with a lifetime of 9.7 ns and QY of 0.75 in TES-Tc, such that the radiative lifetime is ~13 ns, similar to previously reported 11.6-13.2 ns lifetimes in TIPS-Tc in toluene and chloroform.[11,12,34]

3.2 Optical properties of crystals and films

In order to understand the impact of intermolecular interactions on optical absorption and PL in these materials, we first explored R-Tc:PMMA blends (with average R-Tc spacings of d = 2 nm and d = 1 nm), followed by pristine R-Tc films and R-Tc crystals.

3.2.1 Optical absorption

Evolving from solution and dilute blends to pristine films and crystals, clear differences are observed in optical absorption spectra due to the onset of intermolecular interactions in more concentrated systems. The R-Tc:PMMA d = 2 nm films exhibited solution-like absorption. The more concentrated d = 1 nm films exhibited line broadening and some redistribution of the oscillator strength, but no significant spectral shifts (Fig. 2a). Pristine TES-Tc films were amorphous and had absorption spectra similar to those of TES-Tc:PMMA d = 1 nm films. Pristine TBDMS-Tc films, however, were polycrystalline and revealed features closer to those of crystals (Figs. 2a and 3a): an overall redshift, significant line broadening, and more pronounced redistribution of the oscillator strength.

The solution-to-crystal redshift (ΔStoC, here defined as the energy difference between the lowest energy absorption resonances in solution and crystal) is due to non-resonant effects caused by the Coulomb interaction of the molecule with its surrounding and exchange interactions between translationally equivalent molecules. The ΔStoC is 0.19 eV in TBDMS-Tc and 0.15 eV in TES-Tc, similar to that in diF R-ADT (e.g. 0.16 eV in diF TBDMS-ADT) and unsubstituted Tc (0.15-0.23 eV) crystals.[15,35] All crystals exhibit polarization-dependent absorption (Figs. 3a-b, S15, and S16) with the Davydov splitting of the lowest-energy peak of 0.13 eV in TES-Tc and 0.11 eV in TBDMS-Tc, which is larger than 0.08 eV in unsubstituted Tc crystals[35] and similar to ~0.11-0.14 eV in pentacene and dibenzopentacene (DBP) crystals.[36–38] The polarization dependence differs throughout the absorption spectra

(Figs. S15 and S16) due to the states with varying transition dipole moment and nature contributing to absorption at each photon energy,[39] similar to that in diF R-ADT crystals.[15] The 1a and 1b anisotropy is considerably less pronounced in the TBDMS-Tc crystal, which could be in part due to the four molecules per unit cell (Z = 4) in this crystal as compared to Z = 2 in TES-Tc, which makes the analysis difficult due to a complicated peak structure and broadening. Additionally, the TBDMS-Tc crystal packing relative to the substrate (Fig. 1b) consists of stacks of herringbone ('gamma') layers where subsequent layers are reversed relative to the previous, which would result in reduced anisotropy when measuring with light polarized in the substrate plane.

3.2.2 Photoluminescence

Photoluminescence (PL) spectra from R-Tc:PMMA blends (d = 2 nm and 1 nm) and pristine TES-Tc and TBDMS-Tc films under 532 nm excitation (which directly excites the S0-S1 transition), are shown in Figs. 2b-c. In all blends, a new emission band (denoted Sx) appeared, with a dominant feature centered at ~1.86-1.89 eV (658-665 nm) (~0.4 eV lower in energy than S1), a larger width than that of the S1 emission (Tables S3 and S4), and vibronic side bands. The monomer-like S1 emission with the 0-0 line peaked at >2.24 eV (<552 nm) was still present in the blended films; however, its intensity progressively decreased relative to Sx as the R-Tc concentration increased (Fig. 2), partly due to self-absorption and largely due to the formation of domains with enabled SF which quenches S1 PL. While increased aggregation would result in a decrease in the ratio of S1/Sx emission as formation of Sx also quenches S1 PL, this was accompanied by an overall decrease in PL quantum yield (QY) by more than an order of magnitude between d = 2 nm blends and pristine films (Fig. S10). We attribute the drop in the PL QY to the formation of aggregates which enable SF at higher R-Tc concentrations. In particular, formation of dark entangled triplet pair states ^{1}(TT) in the process of SF serves as a competing nonradiative process to both S1 emission and relaxation to the Sx state, thus suppressing all competitive emissive processes.

In TES-Tc crystals, the PL spectra were also dominated by a low-energy Sx emission in the 630-750 nm region (Fig. 3c), although the spectra were considerably broader and the QY was more than an order of magnitude lower than in pristine films. Similar features were also observed in PL spectra of TMS-Tc and tBu-Tc films and crystals (Figs. S11 and S19), which have 'slip-stack' molecular packing similar to that of TES-Tc. Excitation of both TES-Tc films and crystals, as well as TMS-Tc and tBu-Tc crystals, at 633 nm, which

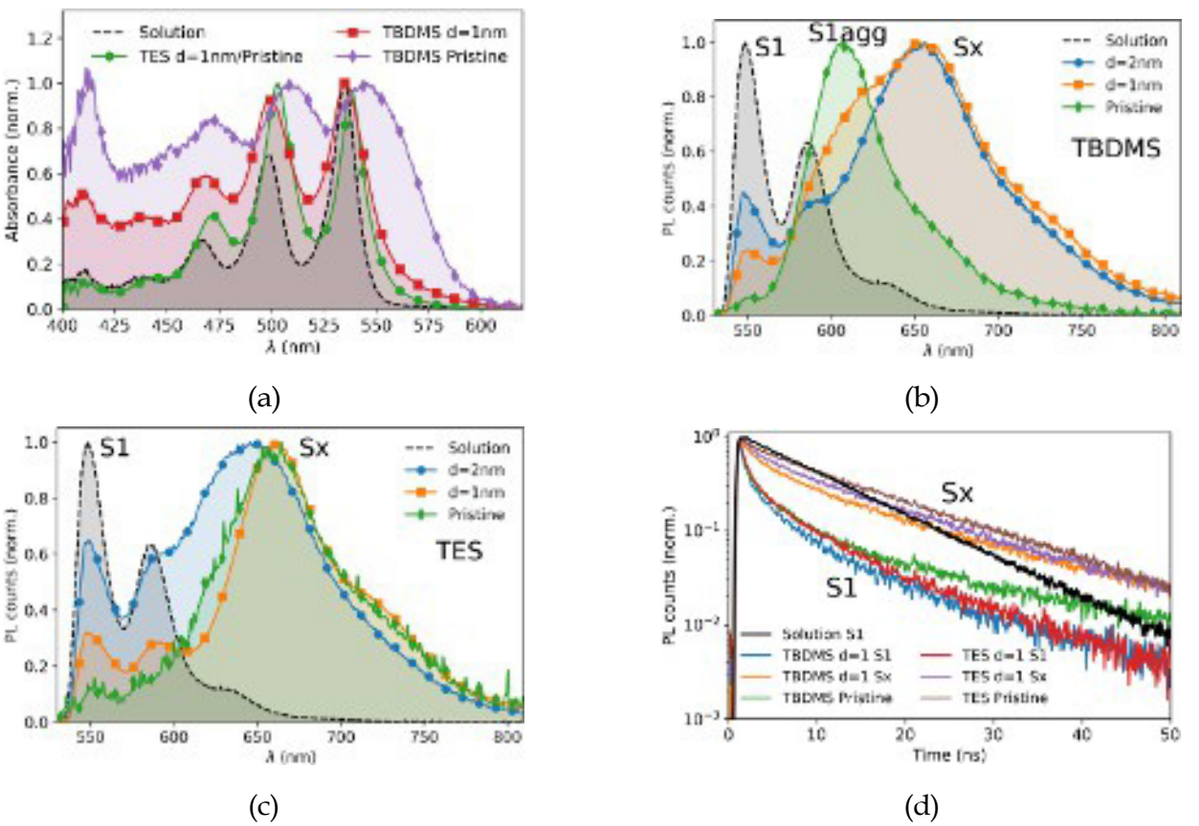

Figure 2: a) Optical absorption spectra of TES-Tc in dilute toluene solution and R-Tc (R = TES, TBDMS) in R-Tc:PMMA (d = 1 nm) blends and pristine films. b) PL of TBDMS-Tc in dilute toluene solution, TBDMS-Tc:PMMA (d = 1 nm and 2 nm) blends, and pristine film. c) PL of TES-Tc in dilute toluene solution, TBDMS-Tc:PMMA (d = 1 nm and 2 nm) blends, and pristine film. d) PL lifetime decays for TES-Tc solution and R-Tc (R = TES, TBDMS) R-Tc:PMMA (d = 1 nm) blends and pristine films. In all blends and pristine films, the PL decays were spectrally filtered to separately probe S1 (540-570 nm) and Sx (630-670 nm) emission (Fig. S12). Symbols in a)-c) are added for clarity.

is considerably below the S0-S1 energy and thus excites the sub-bandgap defect states,[10,40] showed that the Sx emission can be excited directly (Fig. S13). Therefore, we attribute the >650 nm emission to that from low-energy defect states. Similar emissive defects have been observed in anthracene, diphenyl tetracene, DBP, diphenylhexatriene (DPH), and functionalized pentacene crystals.[10,40–43] Because of the similarity of this Sx emission with that in dilute R-Tc:PMMA blends (d = 2 nm) of all R-Tc derivatives under study (regardless of the differences in long-range molecular packing), the Sx emission with vibronic structure could be caused by dimer-like defects with properties largely independent of long-range packing. This is corroborated by similar difference in optical properties between previously studied in unsubstituted tetracene monomers and physical dimers where ~70 nm (0.34 eV) shifts were observed between the 0-0 emission energies of the monomer and dimer species,[44–47] similar to the energy offset between 0-0 S1 emission energy for the monomer and Sx energy (~0.39 eV) in films for the R-Tc derivatives.

This hypothesis is also consistent with observations in TBDMS-Tc in Fig. 2b, where the ~660 nm-peaked Sx emission, dominant in TBDMS-Tc:PMMA blends with d = 2 nm, becomes less dominant and is gradually replaced by a ~616 nm-peaked (~2.01 eV) emission as the molecular concentration increases in d = 1 nm and pristine films (Table S4), upon formation of crystalline domains. This emission will be referred to as 'aggregate emission', denoted as S1agg. The S1agg emission is dominant in TBDMS-Tc crystals (Fig. 3c), where its packing motif (Fig.1b) is not conducive to the formation of Sx states. In contrast, in TES-Tc and other crystals with 'slip-stack' packing of closer-spaced molecules, the S1agg emission is suppressed in fresh crystals, and it becomes significant only when competing processes were disabled in the process of photodegradation (Sec. 3.3).

In order to better understand the nature of the emissive states, the PL lifetimes of S1 and Sx states were separately measured in all films (Fig. 2d). The lifetimes and corresponding weights obtained for each band from bi-exponential fits to the decay dynamics for all films studied are included in Table S5. In TES-Tc:PMMA and TBDMS-Tc:PMMA blends and pristine TES-Tc films, the bi-exponential fits to the decay dynamics revealed the dominant component with a lifetime of 13.8 ns in the Sx emission region (630-670 nm). The lifetimes of the S1 emission in the 540-570 nm region were decreasing with the R-Tc concentration (e.g. from an average lifetime of 3 ns in d = 1 nm TES-Tc:PMMA to 0.6 ns in pristine TES-Tc film), and were considerably shorter than the 9.7 ns S1 lifetime in dilute solutions (Fig. 2d). In crystals, the PL decay dynamics were more complicated, with adequate description of emission in each spectral region requiring a tri-exponential fit function (Fig. S20 and Tables

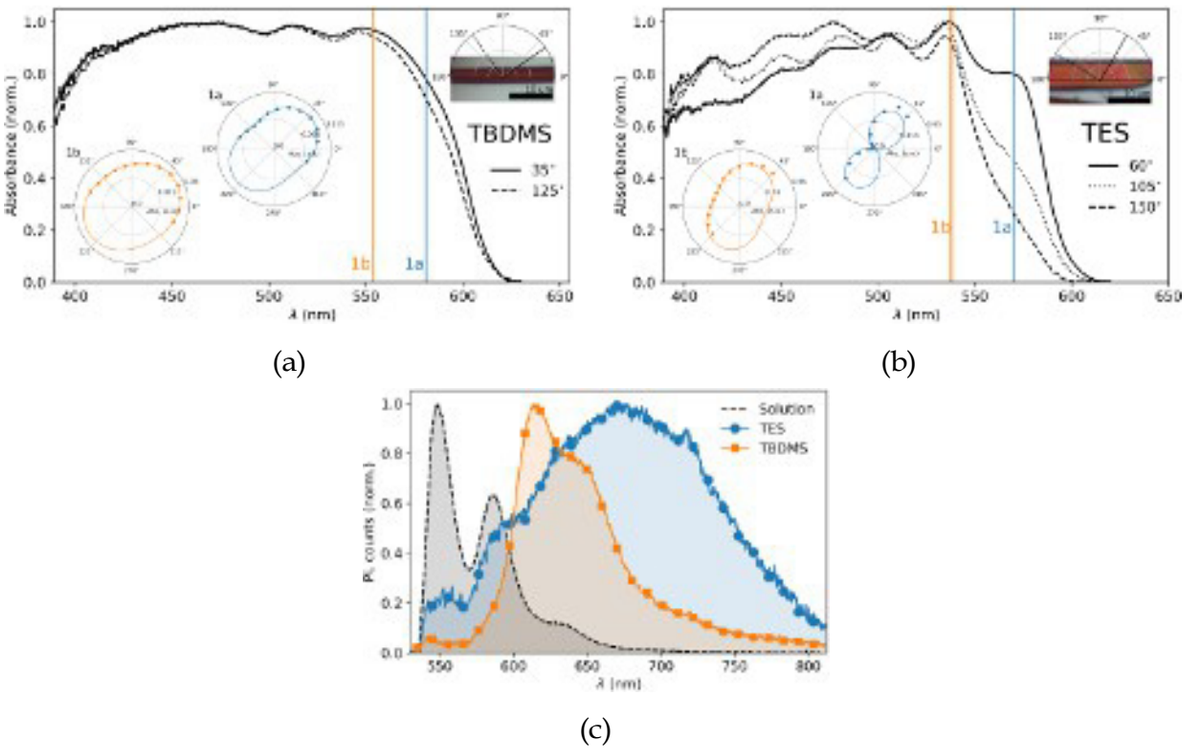

(a) (b)

(c)

Figure 3: Polarization-dependent absorbance in a) TBDMS-Tc and b) TES-Tc crystals. Anisotropy of 1a and 1b features is included in the inset along with the pictures of the crystals. c) PL spectra of TBMDS-Tc and TES-Tc crystals at 300 K. PL spectrum from a dilute TES-Tc solution is also included.

S8 and S9).

3.2.3 Temperature-Dependent Photoluminescence

The dependence of PL spectra and dynamics on temperature for TBDMS-Tc and TES-Tc crystals obtained at 532 nm cw excitation and 515 nm pulsed excitation, respectively, are shown in Figs. 4 and 5 (TMS-Tc and tBu-Tc crystal data in Figs. S19 and S22). The PL lifetimes obtained from bi- or tri-exponential fits to lifetime decays of spectrally filtered bands (S1: 533-550 nm, S1agg: 580-620 nm, Sx: 650-700 nm, Sx: 700-800 nm, Fig. S20a) at various temperatures are summarized in Tables S8 and S9. While all crystals had weak emission at room temperature, the emission considerably increased at low temperatures.

TBDMS-Tc The 'gamma'-packed TBDMS-Tc crystals exhibited S1agg emission characterized by a single vibronic progression at all temperatures (Fig. 4a). As the temperature

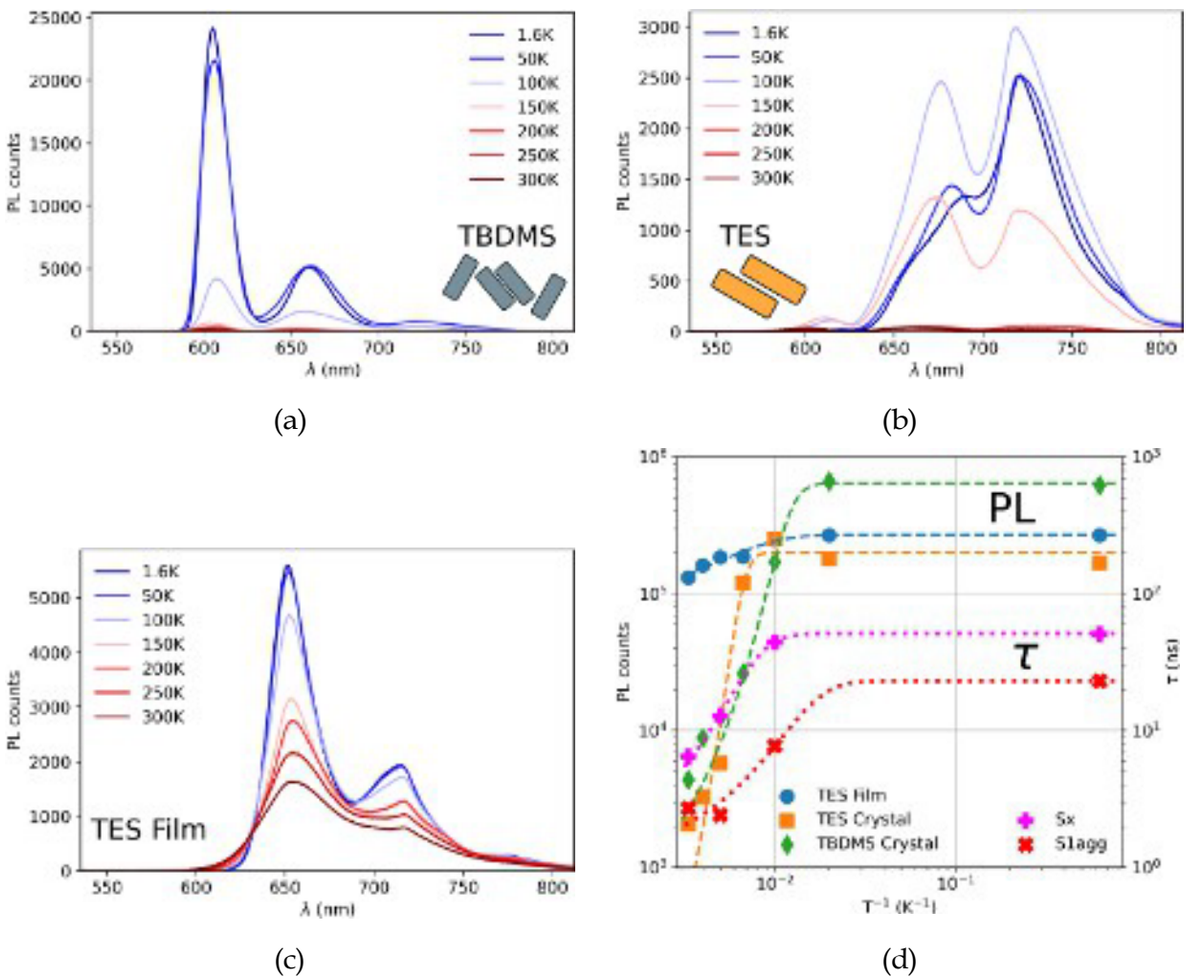

Figure 4: Temperature-dependent PL spectra for a) TBDMS-Tc crystal, b) TES-Tc crystal, and c) TES-Tc amorphous pristine film. d) Integrated PL from S1agg (TBDMS-Tc crystal), Sx (TES-Tc crystal), and Sx (TES-Tc amorphous film) vs temperature. Insets show unit cell cartoon for TES-Tc and TBDMS-Tc crystals. Average lifetime τ vs temperature for Sx and S1agg states in TES-Tc and TBDMS-Tc crystals is also included in d) highlighting that the crystal steady-state PL has over an order of magnitude stronger temperature-dependence than the PL lifetimes.

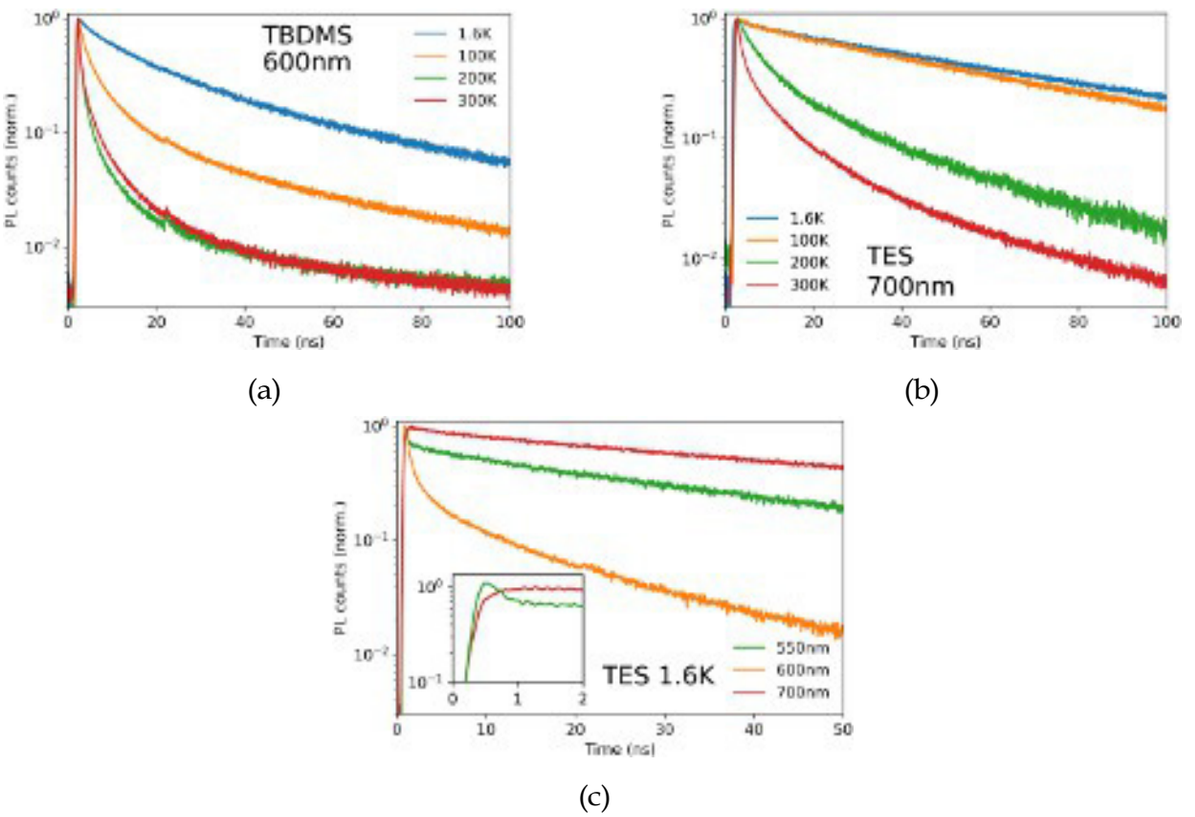

Figure 5: PL lifetime decays for: a) TBDMS-Tc S1agg ('600 nm') emission and b) TES-Tc Sx ('700 nm') emission at various temperatures. c) PL lifetime decays for TES-Tc crystal at 1.6 K for S1 ('550nm'), S1agg ('600nm'), and Sx ('700nm') spectral bands. Long ~60 ns decay component is present in both Sx and S1 emission highlighting their kinetic connection to the ^{1}(TT) states. The inset shows a close up of the early-time dynamics for S1 and Sx, with a delayed Sx rise as it populates from S1 and similar to S1 long-time decay due to delayed PL.

decreased, the steady-state emission intensity increased by two orders of magnitude (a factor of >200) in the 50-300 K temperature range before levelling off below 50 K. This change was accompanied by a change in PL lifetimes (Figs. 4d and 5a) such that the average lifetime increased by a factor of 8.5 from 300 K to 1.6 K, largely due to the appearance of long-lived decay components with lifetimes of ~30-40 ns at 100 K and below (Table S9).

The temperature-dependent spectra of the S1agg state exhibited behavior consistent with superradiance observed in unsubstituted tetracene crystals,[48] which originates from highly delocalized excitonic states in J-aggregates[49] due to the 0-0 oscillator strength scaling with the number of coherent molecules. The identifying feature of this type of superradiance is the temperature-dependent 0-0/0-1 peak ratios, where higher exciton delocalization results in a larger 0-0/0-1 ratio, and the ratio increases as the temperature decreases; this trend is observed in the S1agg emission from TBDMS-Tc crystals which exhibits a factor of 2.5 larger 0-0/0-1 ratio at 1.6 K than at 300 K.

TES-Tc The 'slip-stacked' TES-Tc crystals exhibited emission from low-energy (>650 nm) Sx states (Fig. 4b) which, similarly to the S1agg emission in TBDMS-Tc crystals, increased by two orders of magnitude (a factor of ~150) in intensity and by a factor of 8 in average Sx lifetimes from 300 K to 1.6 K, with the longest lifetime decay components reaching 50-60 ns at 100 K and below (Figs. 4d and 5b, Table S8). The temperature dependence of the minor S1agg emission in the 600-630 nm region was considerably weaker than that of the Sx emission and that of the S1agg emission in TBDMS-Tc crystals, with the average lifetimes only slightly temperature dependent (Table S8). Finally, a residual emission in the S1 region (≤550 nm) was observed with average lifetime decay similar to that of the Sx emission (Fig. 5c) at 100 K and below, exhibiting long lifetime components in the 50-60 ns range. The inset in Fig. 5c shows a delayed rise in the 700 nm 'Sx' emission with a concurrent decay in the ≤550 nm 'S1' emission, implying that the 'S1' population is converted to the 'Sx' species. Qualitatively similar trends are observed in crystals of other 'slip-stacked' derivatives, TMS-Tc and tBu-Tc, with the dominant Sx emission stronger than that in TES-Tc at 300 K and increasing as the temperature is lowered (Fig. S19). Similar to TES-Tc, the S1 and Sx emission in TMS-Tc and tBu-Tc crystals develop components with 40-60 ns lifetimes at low temperatures (Fig. S22).

A higher room-temperature PL QY and considerably weaker temperature dependence were observed in Sx emission from amorphous TES-Tc films (Fig. 4c), with only a factor of ~2 change in steady-state PL intensity across the entire temperature range. Unlike crys-

talline TES-Tc, which exhibited a more complicated Sx spectral evolution with temperature (Fig. 4b), the Sx PL in the film could be well described by a single vibronic progression peaked at ~658 nm (1.88 eV) at all temperatures and an about 25% increase in the 0-0/0-1 peak ratio in the 300 K - 1.6 K temperature range. The 0-0/0-1 ratio is also low (~2) even at 1.6 K (considerably lower that that in the TBDMS-Tc crystal in Fig. 4a), which is consistent with a J-aggregate-like dimer behavior where the exciton is primarily delocalized over two molecules.[50]

To quantify the temperature (T) dependence of the PL yield and lifetimes in Fig. 4d and relate them to the literature, we first used the simplest model (Eqs. S4-S5) for describing steady-state emission and PL lifetimes in the presence of temperature-independent radiative and temperature-activated Arrhenius nonradiative rates with activation energies E_a. For the steady-state emission, the fits yield an activation energy $E_{a,PL}$ of 58 meV for the S1agg emission in TBDMS-Tc crystals and 156 meV and 27 meV for the Sx emission in TES-Tc crystals and amorphous films, respectively. PL lifetimes exhibited considerably weaker temperature dependence than the steady-state PL (Fig. 4d), with activation energies $E_{a,\tau}$ for the average lifetimes of 21 meV and 50 meV in TBDMS-Tc and TES-Tc crystals, respectively. Although at least three time constants are needed to describe the PL dynamics in each spectral range at temperatures above 1.6 K (Tables S8 and S9), emission with the longest lifetime with 40-60 ns time constants, depending on the crystal packing, dominates the overall PL at low temperatures (100 K and below).

The activation energies in the similar range, extracted from fits to temperature-dependent PL data, were previously observed in other tetracenes. For example, 68 meV was obtained in unsubstituted Tc crystals and attributed to the barrier for the ^{1}(TT) formation,[51] and 20-90 meV barriers were attributed to dissociation of ^{1}(TT) states into ^{1}(T...T) in unsubstituted Tc crystals and TIPS-Tc films.[12,51] A considerably weaker temperature dependence in films as compared to crystals, obtained here for TES-Tc, was also previously observed in unsubstituted Tc (with the activation energies of 55 meV in crystals vs 7 meV in films) and attributed to the differences in the ^{1}(TT) formation process, with a low activation energy in disordered films due to the weakly thermally activated exciton diffusion to hot spots where the SF is efficient.[52] This results in SF in films only occurring from molecule populations close to hot spots which efficiently undergo SF, whereas most molecules are in configurations not suited for SF and instead undergo competitive decay mechanisms such as Sx emission.

3.2.4 Kinetic Model

In order to better understand the role of each thermally activated process in the temperature dependent PL in R-Tc, we constructed a kinetic model as described in Sec. S6, seeking the simplest set of states and rate equations that adequately describes temperature dependence of both steady-state and time-resolved PL with one set of parameters. We started from simple models, which were deemed inadequate (Sec. S6.1), and added complexity until the model accurately recreated main features of both the steady-state and time-resolved PL data. In this model, initial excitation of S1 state (state 1 with population N_1) can relax directly to the ground state (with a rate k_1), transition to ^{1}(TT) (state 2 with population N_2) with a rate $k_{12} = k_{12,a} + k_{12,b} \exp(-E_{a,12}/k_B T)$, or form an emissive state S1agg in TBDMS-Tc or Sx in TES-Tc (state 3 with population N_3) with a rate k_{13}.[53] The ^{1}(TT) state can dissociate into two uncorrelated triplet states (state 4) with a rate $k_{24} = k_{24,a} + k_{24,b} exp(-E_{a,24}/k_B T)$) or fuse back into S1 with a rate k_{21}. The emissive states decay with a rate $k_3 = k_{3,a} + k_{3,b} exp(-E_{a,3}/k_B T)$ which accounts for thermally-activated nonradiative processes unrelated to SF. The rate equations (Eqs. S6) and steady-state and time-dependent populations of S1, S1agg or Sx, and ^{1}(TT) states depending on various parameters are detailed in the Supplementary Material Sec. S6. The simulated transients superimposed on the time-resolved PL data (limited by a ~200 ps IRF of our experimental setup) in TBDMS-Tc and TES-Tc crystals are shown in Fig. 6 (steady-state behaviors are shown in the insets), and the rates that best describe the PL data are listed in Fig. S7c and Table S10. The model describes well the steady-state PL behavior of emissive states in the entire 1.6 - 300 K temperature range and PL dynamics at 200 K and below. At 300 K, the model predicts shorter PL lifetime decays as compared to the observed ones (Fig. S25), which suggests that there is an additional process occurring at ns time scales at room temperature contributing to the delayed PL, which is not included in our model. This could be attributed to a combination of factors - the presence of ^{1}(TT) states with different energies (expected in crystals[4,9]) which fuse into S1 on various time-scales, direct ^{1}(TT) → S1agg/Sx pathway, and triplet-triplet annihilation of T1 excitons (T1+T1→^{1}(TT)→S1→S1agg/Sx) - contributing to delayed PL at high temperatures but inefficient at 200 K and below.

Based on the ultrafast spectroscopy findings for other Tc and similar ADT derivatives,[12,35,54] we assume that the ^{1}(TT) formation occurs at picosecond times scales, which is unresolved in our time-resolved PL experiments, and vary the rates to obtain best agreement with the data across our temperature range of 1.6 - 300 K and understand a considerably stronger temperature dependence of steady-state PL as compared to ns-time-scales dynamics.

We find that the presence of thermal activation in the ^{1}(TT) formation rate k_{12} is necessary for adequately describing the steady-state PL and in the ^{1}(TT) dissociation (towards uncorrelated triplets T1) rate k_{24} for description of temperature dependent PL dynamics. The appearance of the PL lifetime constant in the 40-60 ns range at low temperatures is associated with the rate k_{21} due to the fusion of the ^{1}(TT) states to recreate the S1 state, which then repopulates S1agg in TBDMS-Tc or Sx in TES-Tc at longer times resulting in matching long-time decays of S1 and S1agg or Sx (inset of Fig. 5c and Fig. S21). Additionally, the rate k_3 is also temperature dependent due to thermally activated nonradiative decay of S1agg or Sx state (state 3 in the model), depending on the crystal, via processes unrelated to SF. The presence of this process can be inferred via, for example, temperature dependent PL (with an activation energy of ~50 meV) from Sx states in amorphous TES-Tc films under 633 nm excitation, which excites Sx states directly and does not initiate SF (Fig. S13 and Table S7).

The modeling revealed the presence of both non-activated ^{1}(TT) formation pathway ($k_{12,a}$) and a thermally activated path with $E_{a,12}$ of 50±27 meV and 55±13 meV in TBDMS-Tc and TES-Tc crystals, respectively. The ^{1}(TT) dissociation barrier in TBDMS-Tc at 85±10 meV is lower than 130±3 meV in TES-Tc, which we attribute to the specifics of molecular packing of these derivatives, as discussed in Sec. 4.2. The maximal populations of ^{1}(TT) pairs and T1 production yields (T1 population at t = 200 ns, assuming no decay from T1 reservoir) are higher in TES-Tc at all temperatures, with the largest differences at low temperatures (<150 K) and more comparable TT/T1 generation at higher temperatures (Fig. 7). At 300 K, the kinetic model predicts an upper limit of T1 QYs of 191±2% for TES-Tc and 181±4% for TBDMS-Tc. Although these yields are lower at low temperatures, even at 1.6 K both TES-Tc and TBDMS-Tc are producing T1 excitons via SF, with upper limits of 58±6% and 29±4% QYs, respectively.

3.2.5 Magnetic Field Effects

To further investigate how the emissive states observed via PL measurements participate in or affect the SF dynamics, we studied the magnetic field (B-field) dependence of the steady-state PL and PL dynamics in the 0-7 T range (Figs. 8 and 9) at various temperatures. Similar trends were observed in the emission from S1agg in TBDMS-Tc and Sx in TES-Tc crystals (Fig. 8): the PL emission obtained under 532 nm excitation decreased from the initial 0 T yield at low fields (<2 T), with magnetic field effects (MFE = $(PL(B) - PL(0))/PL(0)$) reaching -0.05. At higher fields, the PL yield increased to above the 0 T

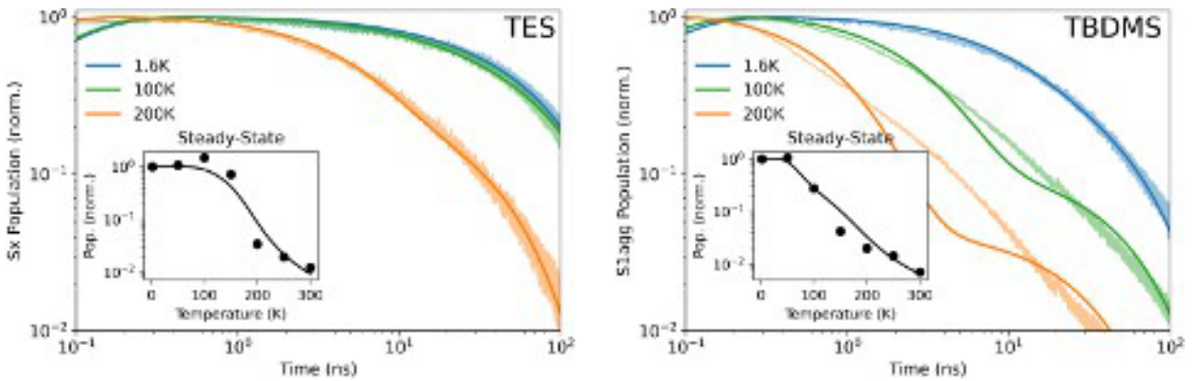

(a) (b)

Figure 6: Time-dependent and steady state (inset) solution to the kinetic model described in the text (Eqs. S6) compared to the experimental PL data for a) Sx emission in TES-Tc and b) S1agg emission in TBDMS-Tc crystals. The calculated Sx (TES-Tc) and S1agg (TBDMS-Tc) population dynamics are overlaid on the measured PL lifetime decays for those bands for each temperature. The model accurately recreates observed time-resolved behavior at 200 K and below and steady state behavior at 1.6 - 300 K.

yield, reaching positive MFEs of ~0.5 (TBDMS-Tc) and ~0.2 (TES-Tc) at 7 T at 100 K. At 1.6 K, qualitatively similar behavior was observed, but the turnover from decreasing to increasing PL occurred at higher B-fields and the increase in PL was considerably less pronounced, with MFE of only ~0.1 in TBDMS-Tc and TES-Tc at higher B-fields (Fig. S24). Similar behavior was observed in TMS-Tc and tBu-Tc crystals, with all four R-Tc crystals exhibiting positive trends in the MFEs at high B-fields at 1.6 K (Fig. 8c). This is consistent with existence of a temperature-independent SF pathway (in addition to temperature-dependent SF), accounted for by $k_{12,a}$ and $k_{24,a}$ rates in our kinetic model, discussed above.

In contrast to notable MFEs in the Sx emission of TES-Tc crystals under 532 nm excitation, no MFEs were observed under 639 nm excitation (Fig. S23a), confirming that direct excitation of Sx does not form ^{1}(TT) states and the MFEs in the Sx PL at 532 nm excitation are due to the state's kinetic connection to ^{1}(TT) via S1, as predicted by our kinetic model (Fig. S23b). Similar observation was previously made in DPH crystals with Sx emission from trap states.[10]

In amorphous TES-Tc films, the Sx PL MFEs at 532 nm excitation were temperature independent and much weaker than in crystals, with a monotonic decrease of PL reaching a MFE of -0.1 at 7 T (Figs. S14 and 8c) and no positive MFEs in our range of B-fields and

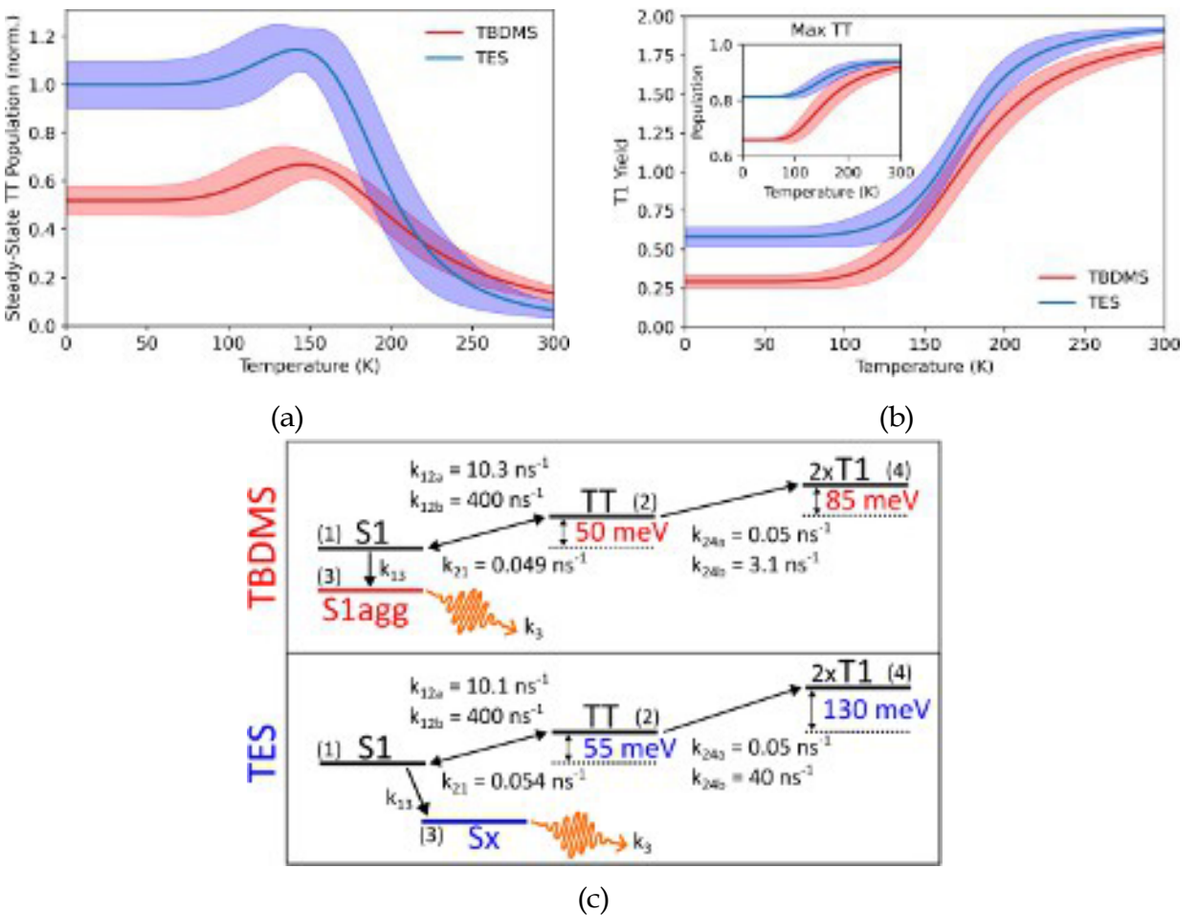

Figure 7: Kinetic model results for a) the steady-state TT population (normalized to the 1.6 K TES-Tc value) vs. temperature and b) predicted T1 yields, calculated as the T1 population at t = 200 ns from an initial population of S1 = 1, assuming no decay from T1. The inset shows the maximal TT population reached from an initial population of S1 = 1. Shaded regions show error calculated from ±20% variation of each parameter (Section S6). c) Energy level diagram for singlet fission in R-Tc, showing the states and transitions used in the kinetic model, along with energy barriers for temperature-dependent TT formation and dissociation rates. Key rates from the model solution are listed, where TT formation and dissociation processes include a temperature-independent rate k_a and temperature-dependent component k_b with activation energy E_a ($k = k_a + k_b \exp(-E_a/k_B T)$).

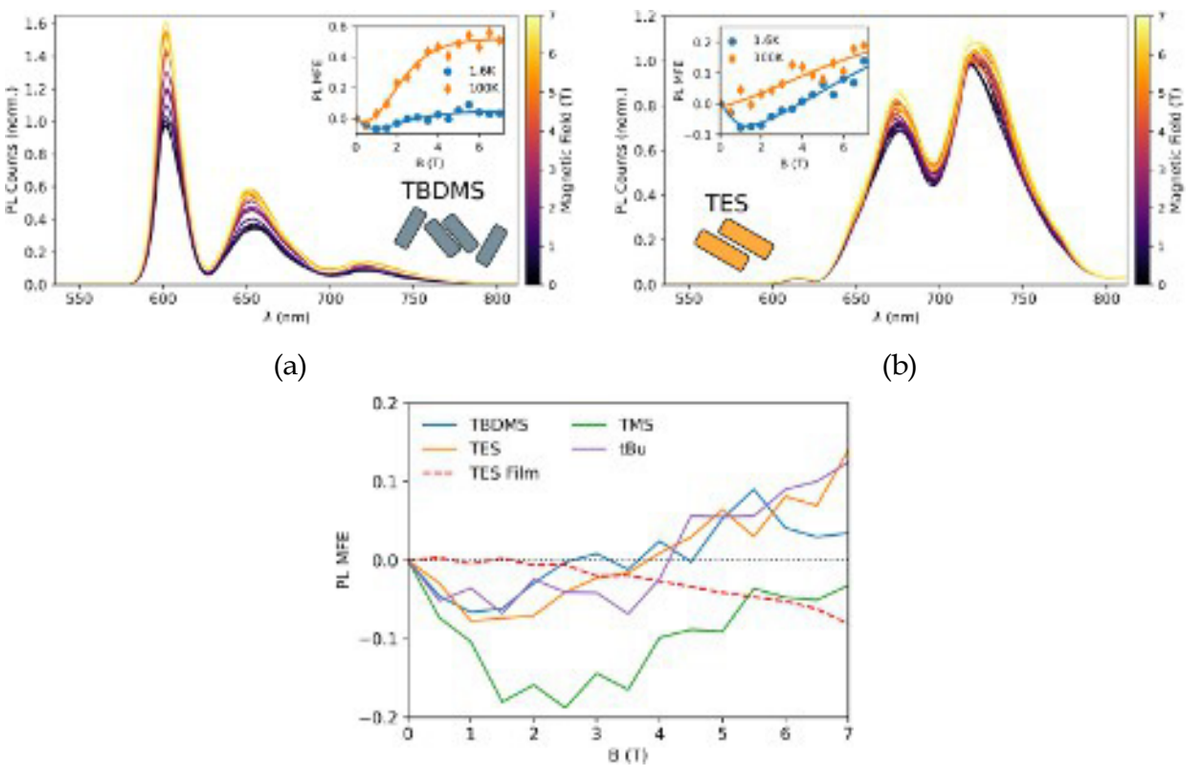

Figure 8: PL spectra vs magnetic field at 100 K for a) TBDMS-Tc and b) TES-Tc crystals, insets are integrated PL vs magnetic field at 1.6 K and 100 K. c) PL MFE for R-Tc crystals (R = TES, TMS, tBu, TBDMS) at 1.6 K which all show positive trends in the MFE due to SF. Data for TES-Tc amorphous film are also included in c) showing a monotonic negative trend in the MFE.

temperatures.

The PL dynamics of S1, S1agg, and Sx states were also affected by strong B-fields (Figs. 9a-b), with the PL lifetimes higher (i.e., PL decays slower) under strong B-fields in the 100-300 K range. The lifetime MFEs ($\tau_{MFE} = (\tau(B) - \tau(0))/\tau(0)$) and τ is the weighted average of three lifetimes for a particular band) were stronger at higher temperatures (inset of Fig. 9a) and for the S1 state.

The B-field dependent PL from singlet states like S1agg and Sx is due to their kinetic connections to the triplet pair states formed in the SF process (Figs. 7 and S23b).[10,55] We associate the observed positive MFEs with the ^{1}(TT) dissociation to spin-mixed pairs ^{1}(T...T)/uncoupled triplet states T1 where the strong B-fields reduce the number of states with singlet character available for transition and affect spin relaxation, consistent with B-field effects on other SF systems in the literature.[1,50,56–60] This effectively results in longer lifetimes of ^{1}(TT) states and higher probability of triplet fusion which reforms the S1 state population, which is observed in all crystals under study. No resonant effects[9,59] due to level crossing between entangled triplet pair states of different spin multiplicity were observed in our experiments, which could be in part due to a resolution of our B-field sweeps insufficient to observe narrow resonances and due to the B-field orientation perpendicular to the substrate which affects the resonant behavior.[61] Additionally, TDDFT methods predict stronger intermolecular interactions (quantified by exciton coupling energies V in dimers extracted from crystal structures) in crystals of all R-Tc derivatives under study as compared to, for example, TIPS-Tc (Tables S18-S22) which has resonances at B-fields in the 3-11 T range.[9] This may lead to higher average exchange coupling energies J in the triplet pairs, shifting resonances to higher B-fields than those in TIPS-Tc,[9] outside of our experimental range of $\leq$7 T.

The presence of B-field-dependent long-lived components in the S1 PL dynamics at low temperatures is consistent with the triplet fusion reforming this state from the triplet pairs generated via non-thermally-activated SF pathway. No quantum beats due to spatially separated triplet pairs that were seen in unsubstituted Tc crystals at ns time scales[62] were observed in any of the crystals under study on our time scales. Therefore, we consider that it is mostly geminate and relatively strongly interacting ^{1}(TT) states that contribute to our delayed PL via triplet fusion described by the rate k_{21} in the kinetic model.

The behavior of the steady-state PL and PL dynamics vs B-field is qualitatively similar to that vs temperature, with high B-fields increasing the effective barrier for ^{1}(TT) separation, similar to the effect of lowering the temperature. This behavior can be empirically

reproduced by introducing a B-field-dependent factor on the rate k_{24} where $k_{24}(T, B) = k_{24}(T) \exp(-B/B_0)$, as shown in Figs. 9c-d and S23b for the 100 K data, with B_0 = 12.4 T for TES-Tc and 0.8 T for TBDMS-Tc. The larger B_0 in TES-Tc may indicate that the ^{1}(TT) pairs formed at 100 K in TES-Tc crystals have on average larger exchange coupling energies J than those in TBMDS-Tc, which require higher B-fields for spin-mixing of the states in the process of triplet pair separation into ^{1}T...T/T1.[60,63,64] This would be consistent with longer ^{1}(TT) lifetimes at lower temperatures (Tables S8 and S9) in TES-Tc (50-60 ns) as compared to TBDMS-Tc (30-40 ns) and TDDFT calculations of exciton coupling energies V (Tables S18 and S20) which predict stronger intermolecular interactions in TES-Tc, potentially enabling formation of ^{1}(TT) states with higher exchange coupling energies J.

The lack of the positive trend in the MFEs of amorphous TES-Tc films is consistent with lower SF yields in films as compared to crystals, with the SF occurring from hot spots with suitable intermolecular orientations[52,65] that are only weakly coupled to the emissive populations, similar to observations in other acenes. Here, the MFEs are most likely dominated by Δg (g-factor anisotropy due to spin-orbit coupling) effects which exhibit negative and monotonic MFEs at high B-fields.[9] This is in contrast to crystals where the positive MFEs due to efficient SF dominate at higher temperatures and only at 1.6 K the negative MFEs are comparable in magnitude to the positive MFEs. The quantitative description of the B-dependent and temperature-dependent MFEs in R-Tc crystals requires further investigation. For example, previous studies inferred mechanisms of spin relaxation during the triplet pair separation from such data using modeling with stochastic Liouville equations and showed how triplet hopping and thermal librations contribute to the interplay of positive and negative MFEs in rubrene films.[64] In our case, however, such interplay occurs at considerably higher B-fields, where additional effects such as that of Δg need to be accounted for.

3.3 Photochemistry

In order to understand the connections between the photophysical and photochemical processes in materials under study, we measured evolution of optical absorption and PL of R-Tc single crystals during either white light illumination (absorption) or a continuous 532 nm excitation (PL) causing formation of endoperoxides (EPOs) in air in 'bottom' samples[16] and photodimerization in vacuum or encapsulated ('top') samples.[20,66] The EPO formation in R-Tc crystals occurred considerably faster than photodimerization at room temperature, as observed in our previous work in TIPS-Tc films.[20] The optical absorption of R-Tc molecules in the visible wavelength range in all films and crystals decreased with photodegradation,

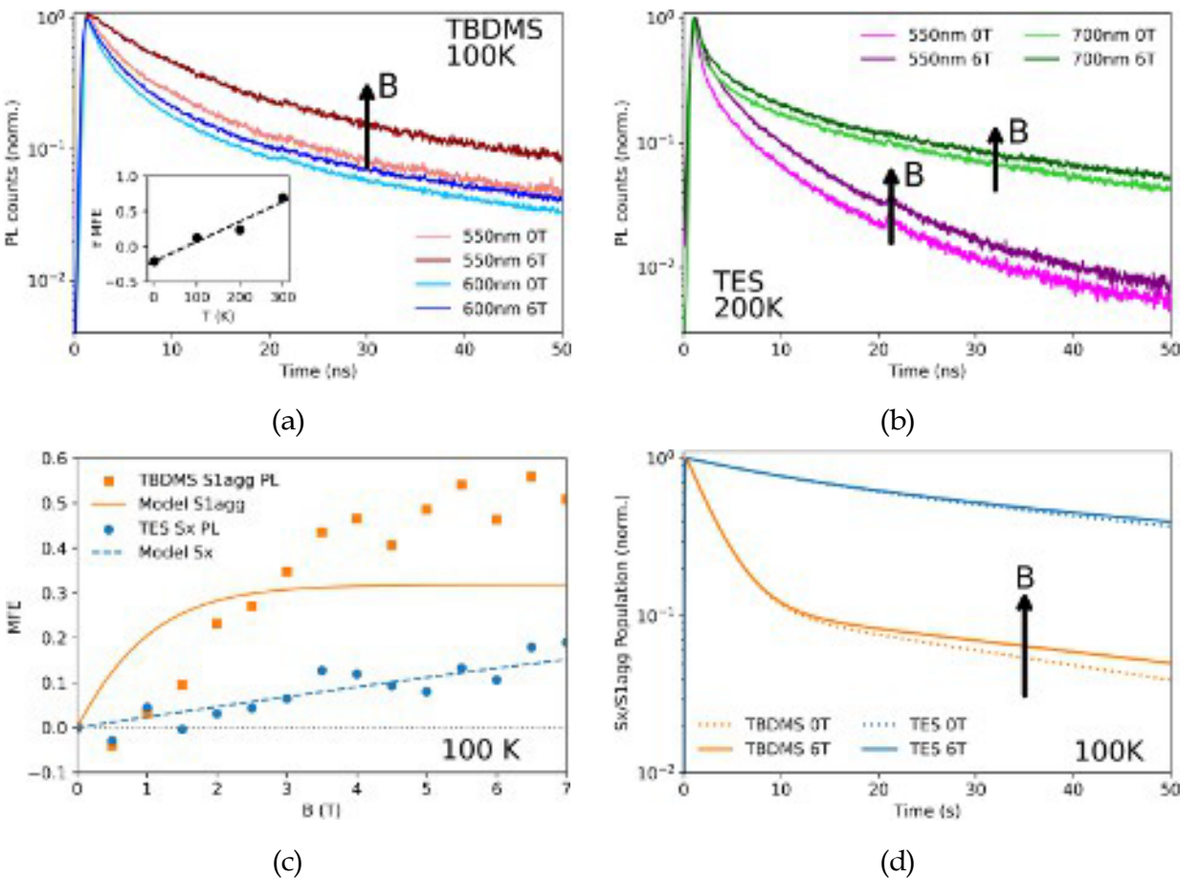

Figure 9: PL lifetime decays in a) TBDMS-Tc crystal at 100K and b) TES-Tc crystal at 200 K, at 0T and 6T, spectrally filtered to isolate emission bands (Fig. S20a): S1 ('550 nm'), S1agg ('600 nm', in TBDMS-Tc) and Sx ('700 nm', in TES-Tc). Inset in a) shows MFE on the average S1agg lifetime in a TBDMS-Tc crystal as a function of temperature. c) Steady-state Sx (S1agg) PL MFE in TES-Tc (TBDMS-Tc) crystals measured at 100 K (data points) overlaid with simulated MFEs (lines) for Sx and S1agg population using steady-state solution in the kinetic model for T = 100 K. d) Simulated MFE on time-dependent solution of kinetic model for Sx (TES-Tc) and S1agg (TBDMS-Tc) showing similar lifetime decay behavior to that in the experimental data.

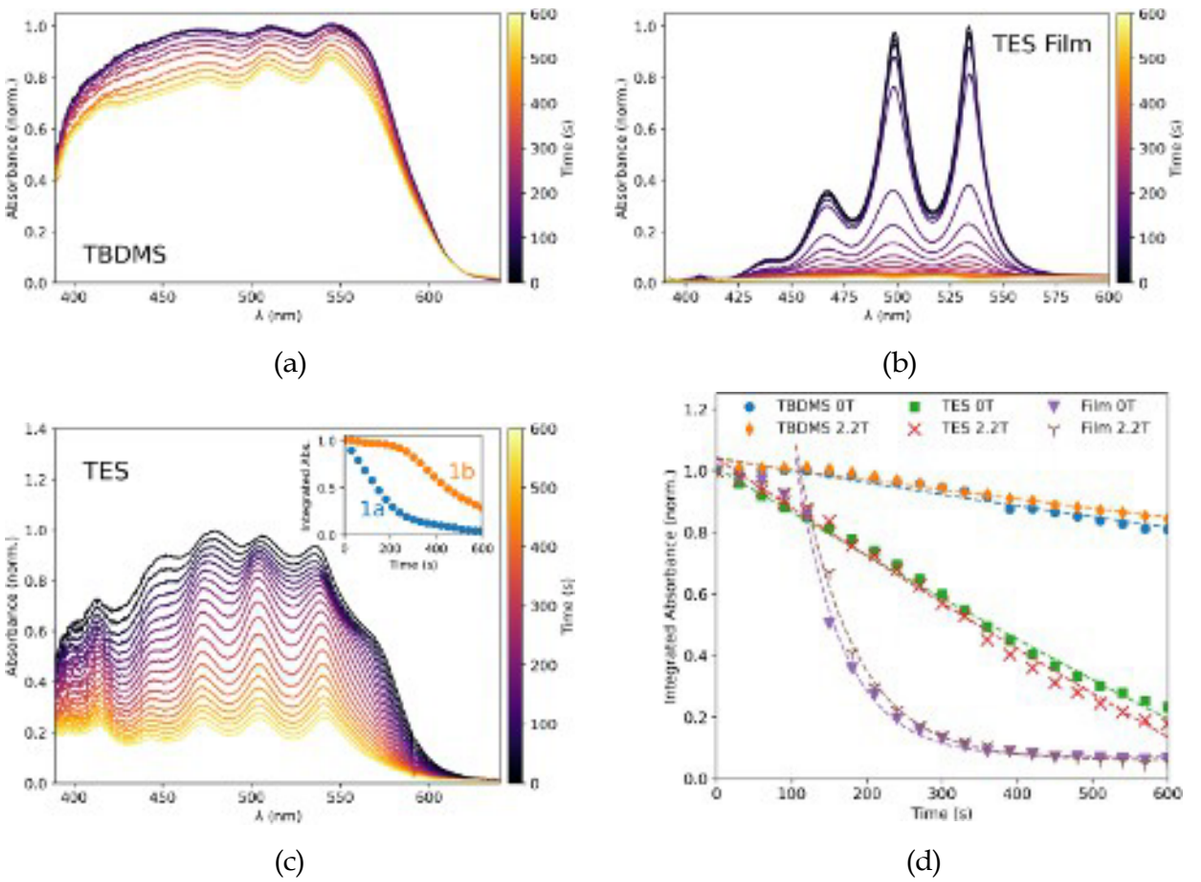

Figure 10: Photodegradation of optical absorption in air in a) TBDMS-Tc crystals, b) amorphous TES-Tc films, and c) TES-Tc crystals under unpolarized white light; inset shows absorption decays of the lower- and higher-energy Davydov components, 1a and 1b. d) Integrated absorption photodegradation at 0 T and 2.2 T for a TBDMS-Tc crystal, TES-Tc crystal, and TES-Tc film. Dashed lines are fits to decays (parameters in Table S23.)

whereas the spectral evolution of PL depended on the system and the photodegradation mechanism, as discussed below.[20,23]

3.3.1 Photodegradation in air: EPO Formation

Figures 10 and 11 show evolution of absorption and PL spectra, respectively, of air-exposed TBDMS-Tc and TES-Tc crystals, as well as of an amorphous TES-Tc film, upon continuous light excitation (50 W/cm^2 of white-light and 40 W/cm^2 of 532 nm for absorption- and PL-based measurements, respectively) at room temperature (300 K), due to photoinduced reactions with oxygen.[16,18,67] In order to quantify the reaction rate constants, we fit

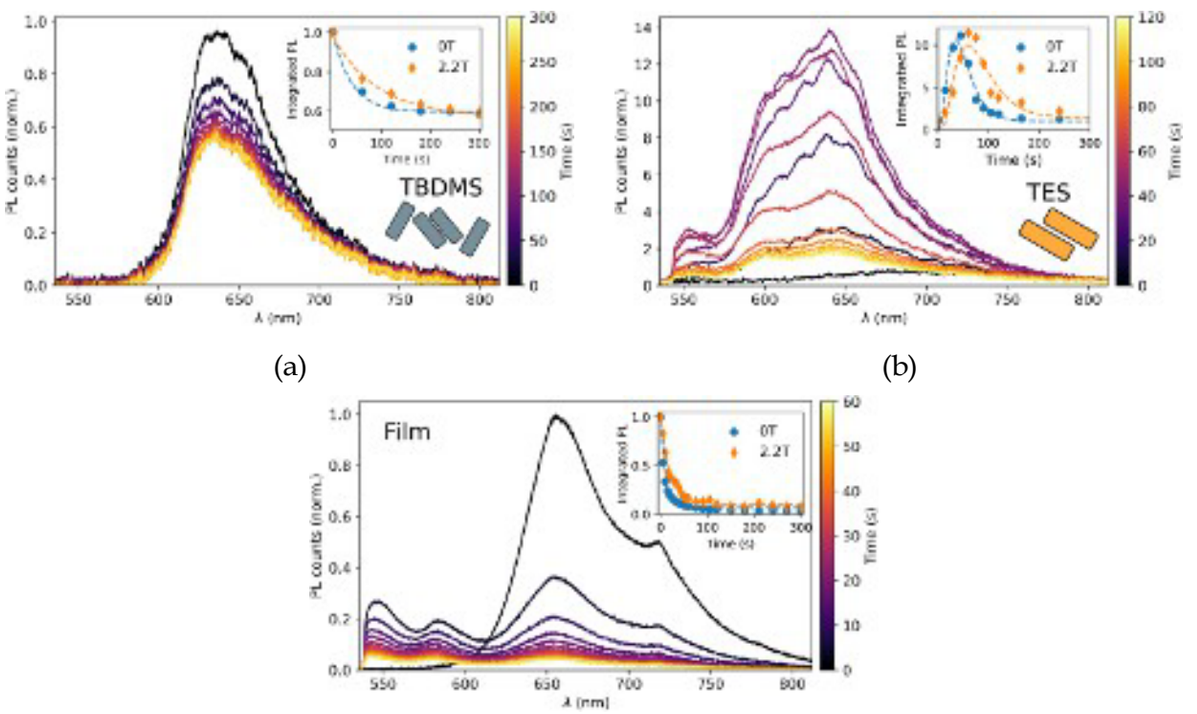

(a) (b)

(c)

Figure 11: Evolution of PL emission due to photodegradation in air in: a) TBDMS-Tc crystal, b) TES-Tc crystal, and c) TES-Tc film under 532 nm cw laser illumination under 40 W/cm^2. Insets show integrated PL over time at 0 T and 2.2 T; dashed lines are fits to decays (parameters in Tables S25-S26).

the decay of the integrated absorption (Fig. 10c) with a monoexponential function (Table S23), which reveals that overall, the TBDMS-Tc crystals are about a factor of 6 more stable than TES-Tc crystals with respect to the EPO formation, with decay time constants of 2460±100 s and 397±20 s, respectively, under the same illumination conditions. The TES-Tc amorphous film is about a factor of 2.5 less stable than the TES-Tc crystal, with the half-life of absorbance decay in films of about 150 s as compared to 355 s in the crystal. Lower stability of amorphous films in air as compared to crystals was previously observed in a variety of organic materials,[68] in part due to a higher oxygen permeability in disordered films.

Interestingly, in TES-Tc crystals, the 1a and 1b features in the absorption spectra (Fig. 10c) had different photodegradation behavior, where 1a decayed considerably faster (half-life of 140 s) and 1b exhibited a slow initial decrease, with rates similar to TBDMS-Tc, followed by a faster decay component (overall half-life of 445 s, inset of Fig. 10c). The amorphous TES-Tc films (where the 1a feature is not present in the spectra) exhibited behavior similar to that of 1b in crystals but with faster dynamics (Fig. 10b,c).

The evolution of the PL spectra during the photodegradation-inducing 532 nm cw illumination (Fig. 11) provides insights into susceptibility of specific molecular populations to photodegradation and shows more complicated behavior than the absorption. In our experiments, emission only in the 540-800 nm wavelength region is monitored, which is due to the parent molecules and does not include any contributions of UV-absorbing photoproducts (such as EPOs) with emission below 500 nm.[20,66]

In 'slip-stacked' crystals such as TES-Tc, the PL evolution during photodegradation involves multiple emissive states.[23] As discussed in Sec. 3.2.2, at room temperature, the dominant PL in freshly made TES-Tc crystals is from the low-energy (>650 nm) Sx states with low QY (<1%). Upon continuous 532 nm illumination, the total PL yield rapidly increases by more than an order of magnitude, with S1 (540-560 nm), S1agg (580-630 nm), and Sx (640-700 nm) emissions growing within the first 40 s after photoexcitation (Fig. 11b) with slightly different rates (Table S25). This PL yield increase is due to the rapid degradation of molecules in configurations conducive to dark ^{1}(TT) and T1 states formation, which reduces the probability for SF and enhances PL by populating various emissive states instead.[20,23] This is followed by the decrease in PL from all emissive states as the molecules participating in populating the emissive states and the emissive species themselves undergo degradation (Table S25). In TES-Tc amorphous films under the same illumination conditions, there are considerably fewer molecules in the dark states and so the increase in the PL emission is

considerably less pronounced than in TES-Tc crystals. Instead, the dominant effect is the fast decay of the Sx emission (630-750 nm) within the first ~10 s of illumination, similar to that in TIPS-Tc films,[20] with the S1 (540-550 nm) emission only slightly increasing before decreasing (Fig. 11c).

In TBDMS-Tc crystals, the nature of PL evolution during the photodegradation depends on the photodegradation-inducing light intensity. At 40 W/cm^2 (same as used for TES-Tc crystal in Fig. 11b), a monotonic decrease in S1agg PL (>600 nm) is observed during the degradation, with no evidence of an increase in emission from other states (Fig. 11a). The parameter y_0 which describes the fraction of the initially emissive population that remains emissive (obtained from a monoexponential fit to the PL decay in the inset of Fig.11a, Table S26) is about 0.6, which means that 60% of emissive TBDMS-Tc molecules and/or molecules that populate that state are not susceptible to the photodegradation under these illumination conditions in air. The emissive population, however, constitutes only a small subset of the overall TBDMS-Tc population (PL QY of <1%) at room temperature, and it is possible that considerably smaller percentage of the overall population is expected to stay intact after a long irradiation time period in air (e.g., ~4-7% in TIPS-Tc[20] and ~7% in TES-Tc films). At higher illumination intensities, a qualitatively similar to TES-Tc crystals behavior, with an initial rise in both S1agg and S1 emission, is observed in TBDMS-Tc crystals (Fig. S33), which is further discussed in Sec. S8.1.

The photodegradation of R-Tc in air involves generation of reactive oxygen species followed by a chemical reaction to form an EPO, with both of these steps potentially spin-selective. Therefore, they are expected to be sensitive to the the SF efficiency and T1 dynamics, as discussed in Sec. 4.3.1.[16,18] In order to investigate this, we performed the photodegradation experiments with an applied B-field.

The EPO formation in TBDMS-Tc crystals probed via absorption decay was about 25% slower under the B-field of 2.2 T as compared to that in the absence of B-field (Fig. 10d). The PL emission is more sensitive to the B-field, and fitting the integrated S1agg PL photodegradation-induced decay to a monoexponential function, we find the degradation rate is a factor of ~2 slower at 2.2 T than at 0 T. Relatively strong B-field dependence of the EPO formation was also observed in the PL of TES-Tc crystals, where overall PL dynamics were about 50% slower at 2.2 T as compared to those at 0 T (inset of Fig.11b and Table S25). This includes longer rise time (20% →80% of the max) of 30 s vs 19 s, time to reach max PL of 65 s vs 40 s, and PL half-life time of 32 s vs 24 s at 2.2 T vs 0 T.

The pronounced B-field effect observed in the PL degradation is consistent with relatively

large MFEs observed in S1agg and Sx PL in R-Tc crystals (Fig. 8) due to these states' kinetic connection to the SF process. The slower rates under B-field are consistent with a less efficient ^{1}(TT) separation into triplet excitons T1 in high B-fields inferred from the MFE PL data, with fewer molecules in T1 states leading to a slower singlet oxygen generation via Type II mechanism relying on T1 states[16] and thus slower photo-oxidation reaction. However, if EPO formation requires T1 states produced via SF, the photodegradation rates should decrease as the sample degrades and SF pathways are destroyed. Instead of this, we see continued degradation of molecules emitting from singlet states (S1/S1agg) after SF yields diminish (which manifests into the PL decrease following the increase with comparable rates (Table S25). This suggests that there is a degradation pathway that does not rely on the SF, for example a singlet state mediated process of oxygen sensitization which can form the precursor states, $^1O_2$ and T1, for the EPO formation. Sensitization of the S1 state in TIPS-Tc with oxygen has been identified as an important pathway for the production of both EPO precursors,[18] which can subsequently catalyze the chemical reactions to form EPOs, as discussed further in Section 4.3.1.

Interestingly, about a factor of 2 slowing down of the degradation rate constant at 2.2 T as compared to 0 T was observed in the Sx PL in TES-Tc amorphous films as well (inset of Fig. 11 and Table S24), even though the PL MFEs were minimal in these films (Fig. S14) at this field. This is consistent with the Sx-emissive molecular populations being distinct and well-separated from SF-enabled 'hot spots'. In this scenario, the high B-field slows down the T1 generation and the production of reactive singlet oxygen via Type II mechanism in the 'hot spots',[16] which in turn slows down the reaction between the singlet oxygen (that diffuses towards emissive species) and the Sx-emitting molecules.

3.3.2 Photodegradation without air: photodimerization

The effects of photodimerization, the dominant photodegradation process in the absence of oxygen,[20,24,44] was investigated both in R-Tc or R-Tc:PMMA films and in R-Tc crystals. The R-Tc:PMMA blends with d = 2 nm had minimal photodimerization due to a large average separation of the R-Tc molecules. In R-Tc:PMMA blends with d = 1 nm, absorption of the parent R-Tc molecules under white-light illumination (which induced the photodimerization) decreased, with no new features forming in the visible spectrum (Fig. S34). Therefore, we consider that the conventional 'butterfly' photodimer, with absorption in the UV region,[44,45,66] is the dominant dimerization product in R-Tc derivatives under study.

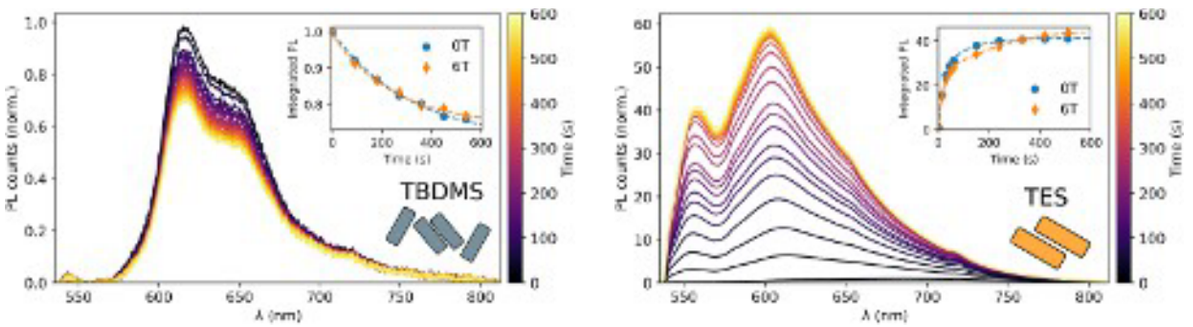

(a) (b)

Figure 12: Evolution of PL due to photodegradation via photodimerization in a) TBDMS-Tc and b) TES-Tc crystals illuminated by cw 532 nm laser. Insets show integrated PL over time at 0 T and 6 T. Dashed lines in inset are fits to decays (fit parameters in Tables S28 and S29).

The PL spectra under a photodimerization-inducing 532 nm excitation in R-Tc:PMMA blended films with d = 1 nm, in which the emission was dominated by the low-energy Sx state (Sec. 3.2.2), exhibited a fast decrease in the Sx emission accompanied by a rise and saturation in S1 emission (Fig. S35). This is consistent with the physical dimer-like species which form Sx and ^{1}(TT) states to be susceptible to photodimerization,[45] causing a reduction in Sx and SF yields. This results in an increase in S1 emission from monomer-like species as sites which would previously emit via Sx or undergo SF now emit from S1 as they lack neighboring undegraded molecules to undergo multi-molecular processes. During photodimerization, the PL yield levels off after a large increase. In contrast, during EPO formation, after the temporary increase, the PL quickly degrades and the S1 emission disappears as more EPOs form. This suggests that while EPO formation has a significant effect on all molecular populations, the S1-emissive molecular population is not particularly susceptible to photodimerization.

In pristine amorphous TES-Tc films, the PL behavior under photodimerization-inducing 532 nm excitation was similar to blended films, and it was further investigated at different temperatures in the 100-300 K range. The photodimerization in these films was thermally activated, with rate constants (obtained from fits to the integrated PL spectral evolution) differing by two orders of magnitude in this temperature range. This temperature dependence was quantified using the Arrhenius function ($k_{\mathrm{dimer}} \sim \exp(-E_{\mathrm{dimer}}/k_{\mathrm{B}}T)$, where k_{dimer} is the faster rate obtained from bi-exponential fits to the time dependence of the integrated PL) with an activation energy E_{dimer} of 61 meV (Fig. S36 and Table S27). The fraction of

non-dimerizable molecules y_0 = 0.18 at 300 K is in the 0.16-0.3 range observed in similar experiments in TIPS-Tc films.[20] The photodimerization of molecules could also be induced by a direct 633 nm excitation of Sx states (Fig. S36), despite minimal absorption at that wavelength, consistent with the high affinity of the molecules responsible for the Sx emission to photodimerization, as expected from molecules in physical dimer-like configurations.[45]

In R-Tc crystals, we found that the white light intensities used for inducing the EPO formation in air for absorption-based measurements did not induce any photodimerization for these samples in vacuum, consistent with photodimerization being considerably slower than the EPO formation.[20] The photodimerization in R-Tc crystals could still be monitored via PL under strong 532 nm excitation at 40 W/cm^2 (same as used in experiments in air for direct comparison), with Fig. 12 (Fig. S37) showing evolution of PL spectra of TBDMS-Tc and TES-Tc (tBu-Tc and TMS-Tc) crystals upon photodimerization. Similar to the EPO formation, the TBDMS-Tc crystals were more stable with respect to photodimerization than other R-Tc crystals. This could be related both to the differences in photophysics and to the positional requirements for the 'butterfly' dimerization which are better met by the molecular arrangements in TES-Tc (as well as tBu- and TMS-Tc) crystals as compared to TBDMS-Tc.[23] In particular, while the same number of pairs per unit volume (~4 per 1.5 nm^3) are in configurations potentially amenable for photodimerization in both TES-Tc and TBMDS-Tc crystals (TBMDS-β, TBMDS-α, and TES-α, Fig. 1b-c, with intermolecular spacing of ~3.3-3.4 Å)[69] the TES-α dimer has a more favorable geometry, with intermolecular short-axis and long-axis slip distances of only 1.31 Å and 2.9 Å, respectively (as compared to 0.89 Å and 6.03 Å in TBDMS-β and 1.48 Å and 8.08 Å in TBDMS-α).

Photodimerization in TBDMS-Tc (Fig. 12a) had similar effects on the PL as the EPO formation, only at longer time scales. The S1agg PL monotonically decreased, with no increase in emission from other states. Monoexponential fits to the decay (Table S28) yield a decay time constant of 318 s, about an order of magnitude slower than that for the EPO formation (Table S26) under the same illumination conditions. The photodimerization was also less B-field dependent than EPO formation, consistent with a predominantly singlet state mediated process or lack of spin state selectivity in the photodimerization process. The fraction of the molecules which contribute to S1agg emission (i.e. those that populate S1agg and emissive S1agg molecules themselves) that are not susceptible to photodimerization, y_0 of ~0.7, was higher than the corresponding parameter for the EPO formation (~0.6), consistent with fewer molecules susceptible to photodimerization as compared to photo-oxidation, due to positional constraints.

The photodimerization of TES-Tc (Fig. 12b) had a qualitatively similar initial PL behavior to that due to EPO formation in air, with the PL increasing the initial yield by a factor of ~40 in the first 200 s of illumination, due to molecules in configurations conducive to forming dark states, such as ^{1}(TT), converting to photodimers and disabling the ^{1}(TT) and T1 formation. Unlike with EPO formation, however, this PL emission levels off at its maximum (inset of Fig. 12b) instead of decaying (inset of Fig. 11b), which indicates that molecules in dark states, and in configurations that favor dimerization, have converted to photodimers, leaving behind molecules in S1 and S1agg states that are not in dimerization-prone orientations. Under a B-field of 6 T, the photodimerization proceeds at a ~2× slower rate, but the fraction of the overall population susceptible to photodimerization increases (Table S29) as compared to 0 T.

Similar to films, in all R-Tc crystals the photodimerization was strongly thermally activated, and no dimerization was observed at or below 100 K under our illumination conditions.

4 Discussion

4.1 Exciton dynamics depending on molecular packing

The R-Tc crystals data are consistent with the model in Fig. 7c with the parameters summarized in Table S10. In crystals of all derivatives, upon 532 nm (S0-S1) excitation, the ^{1}(TT) formation proceeds even at 1.6 K, with an additional thermally activated process depending on the molecular packing. The ^{1}(TT) dissociation also has a temperature-independent and thermally activated components, with the higher thermal barrier and longer ^{1}(TT) lifetimes in a 'slip-stacked' TES-Tc as compared to 'gamma'-packed TBDMS-Tc. At higher temperatures, the steady-state ^{1}(TT) population and the T1 formation rate are comparable in TES-Tc and TBDMS-Tc, whereas TES-Tc packing is more advantageous for SF at lower temperatures (below 150 K). In all R-Tc crystals, the ^{1}(TT) dissociation is partially suppressed by strong B-fields, yielding positive MFEs in PL, which are present even at 1.6 K and increase with temperature.

The presence of thermally activated and temperature-independent ^{1}(TT) formation and dissociation pathways reflects the anisotropy of properties of ^{1}(TT) pairs in R-Tc crystals, where SF could proceed by different mechanisms due to a distribution of exchange coupling energies J and different propensity for stochastic changes of J driven by molecular conformations and lattice vibrations.[70] For example, in TIPS-Tc crystallites, three ^{1}(TT) states with different energies and J values were observed down to 1.4 K,[9] and ultrafast

temperature-independent vibronically coherent ^{1}(TT) formation was promoted by a 760 cm^{-1} vibrational mode[12] (consistent with intramolecular ring deformation[71]). In rubrene, a ps-time scale thermally activated ^{1}(TT) formation was driven by a symmetry-breaking low-frequency ($\sim$100 cm^{-1}) intermolecular torsional mode.[72] Both mechanisms (driven by intermolecular vibrations and intramolecular vibrations or high intermolecular coupling strength to enable thermally-activated and nonactivated ^{1}(TT) formation, respectively) could be relevant for the R-Tc crystals under study. For the ^{1}(TT) dissociation into uncorrelated triplets, the characteristic triplet hopping time is an important parameter,[12] and it varies among different ^{1}(TT) pairs and directions in anisotropic R-Tc crystals. For example, in TIPS-Tc, over four orders of magnitude difference in hopping times (i.e., between 2.5 ps in a π-stacked dimer and 52 ns in a dimer extracted from TIPS-Tc crystal structure) was theoretically predicted depending on the intermolecular orientations.[12] These differences could enable the co-existence of thermally activated and nonactivated mechanisms of ^{1}(TT) dissociation; additional factors are ^{1}(TT) separation via different hopping mechanisms (characterized by different temperature dependence)[73] and CT mediation.[74]

In all R-Tc crystals, the PL emission is low at room temperature, dramatically increasing at low temperatures. In 'slip-stacked' derivatives (TES-, TMS-, and tBu-Tc), the emission (Sx) primarily originates from defect sites with energies red-shifted by $\sim$0.4 eV from the monomer S1 emission. Stronger room-temperature Sx emission was observed in TMS-Tc and tBu-Tc derivatives as compared to TES-Tc, which may suggest that tighter molecular packing of TMS-Tc and tBu-Tc, characterized by larger exciton coupling energies V (Tables S19-S22) in lowest-energy dimers (97 and 94 meV in TMS-a and tBu-β as compared to 78 meV in TES-a) is conducive to dimer-like defect formation. Instead, the 'gamma'-packed TBDMS-Tc with the highest V of only 20 meV exhibited J-aggregate-like emission S1agg, red-shifted by about 0.24 eV from the monomer S1 emission and by about 0.1 eV from the lower-energy Davydov component of absorption. Such J-aggregate-like emission is similar to that in unsubstituted Tc crystals (with a red-shift of 0.32 eV and $\sim$0.1 eV from the S1 monomer emission and the absorption from the lower Davydov component, respectively), which was attributed to intrinsic delocalized exciton emission.[48] Nevertheless, J-aggregate-like defects were also observed in crystalline acenes forming, for example, at dislocation sites,[43] and so the presence of such defects in TBDMS-Tc cannot be ruled out. In spite of different nature of the emissive states in TBDMS-Tc vs TES-, TMS-, and tBu-Tc, there are remarkable similarities in their temperature- and B-field-dependent steady-state emission and PL dynamics behaviors. This is due to their similar role in the overall excited-state

dynamics (Figs. 6 and 7c), where populating these states serves as a parallel channel to the SF, which is not competitive to the SF at room temperature, but becomes highly competitive at low temperatures.

No clear signature of ^{1}(TT) emission previously reported in TIPS-Tc crystals and films was observed.[9,12] The ~650 nm-dominated emission in TIPS-Tc disordered films attributed to ^{1}(TT) emission in Ref.[12] is similar to the Sx emission in our TES-Tc films. However, we showed that we can directly excite this state at 633 nm (Fig. S13) and that upon direct excitation the Sx emission has no B-field dependence (Fig. S23a) implying no participation in the SF process under these conditions.[10] The S1agg emission in TBDMS-Tc could be a candidate for the Herzberg-Teller ^{1}(TT) emission occurring from the 0-n ($n \geq 1$) states,[3] but similarity of its PL behaviors, other than its higher exciton delocalization at low temperatures, to those of Sx in other R-Tc crystals is inconsistent with this state being of a fundamentally different origin. The 560-570 nm-dominated emission which was attributed to ^{1}(TT) states in TIPS-Tc polycrystalline films and crystals,[9,12] was not observed in our R-Tc samples. The ~610-620 nm-dominated S1agg PL is considerably broader than the ^{1}(TT) PL in TIPS-Tc at low temperatures,[9] and S1agg is more than 0.1 eV lower in energy than the TIPS-Tc ^{1}(TT) PL. While it is possible that the ^{1}(TT) state in TBDMS-Tc is slightly lower energy than that in TIPS-Tc based on the DFT calculations, the temperature dependence of the S1agg spectral shape is more consistent with the evolution of a 0-0-dominated J-aggregate emission than with that of the Herzberg-Teller emission,[3] making it unlikely that S1agg is an emissive ^{1}(TT) state in this endothermic system and more likely that it is the relaxed S1 exciton. The S1agg emission is suppressed in TES-Tc due to efficient SF and relaxation to the low-energy Sx states in fresh crystals, but is observed in partially degraded samples (Figs. 11 and 12). Weak ~550 nm S1 exciton emission was also detected in all R-Tc crystals at most temperatures, exhibiting long PL lifetimes at low temperatures, similar to those in Sx and S1agg, and strongest MFE in the PL dynamics (Fig. 9), indicative of the strongest kinetic connection of this state with ^{1}(TT), of all emissive states.

4.2 Comparison with DFT

TDDFT calculations (CAM-B3LYP/6-31+G*) provide several insights into our experimental observations. On the monomer level, all R-Tc derivatives under study have a similar calculated energy difference between the singlet state S1 and double of the triplet state T1: $2E(T1)-E(S1) = 0.11\text{-}0.14$ eV, with both TES-Tc and TBDMS-Tc at 0.11 eV in the optimized geometry. This would make them slightly endothermic SF materials, with SF

activation barriers lower than the 0.16 eV and 0.23 eV similarly predicted for TIPS-Tc and unsubstituted Tc (Tables S12-S15). The energies of Tn states (n = 1, 2, 3) are similar among all R-Tc derivatives (Table S16), suggesting that any losses due to intersystem crossing (ISC) (which are promoted by T1/T2 and S1 or ^{3}(TT) energy alignment),[34,75] would be similar in these derivatives.

Comparison of lowest-energy transitions in dimers generated from the crystal structures of R-Tc derivatives (Tables S18-S22) reveal that TBDMS-Tc supports the formation of dimers with optically bright transitions with a spread of energies, including a lower-energy Frenkel-charge transfer (CT) state at 2.43 eV with the oscillator strength f = 0.4 in TBDMS-β (lower by 0.06 eV than the calculated monomer energy). In contrast, the optically bright TES-Tc dimer states have energies close to/higher than those of the monomer (e.g., 2.51 eV Frenkel state with f = 0.7 in TES-γ, higher by 0.02 eV than the monomer energy, Fig. S18 and Table S20), with dark (f <0.0001) lower-energy dimer states. Generalizing to other 'slip-stacked' R-Tc derivatives, TES-, TMS-, and tBu-Tc all have at least one low-energy dimer state with a $\leq$0.0001 oscillator strength, Frenkel-CT character, and larger energy offset from the monomer energy than TBDMS-Tc (e.g., 2.37 eV in TES-α and 2.24 eV in TMS-α offset by 0.12 eV and 0.16 eV, respectively, from the monomer energy, Tables S20 and S22). Based on our observation of Sx PL in the 'slip-stacked' crystals, we hypothesize that a defect formed on these lowest-energy dimers (e.g. with a decreased intermolecular distance and increased slip along the short molecular axis in a π-stacked pair) could further lower the energy and create a state responsible for low-energy Sx emission in 'slip-stacked' TES-, TMS-, and tBu-Tc crystals.[76] We also note that the explicit inclusion of the surrounding crystal environment would serve to redshift the low-lying singlet states even further. A previous study from one of the authors found that in pentacene derivatives exhibiting a herringbone packing structure, explicit inclusion of the environment leads to redshifts in S1 on the order of nearly 0.1 eV.[77]

Importantly, the lower-energy states in dimers extracted from crystal structures of all R-Tc derivatives under study have a mixed Frenkel-CT character (Tables S18-S22), which has been shown to enhance the Davydov splitting and SF.[49,78] The Frenkel-CT admixture could further mediate the ^{1}(TT) formation,[79] in addition to the mechanisms relying on intra- and intermolecular vibrations discussed above. In contrast, TIPS-Tc crystal structure supports dimers of primarily Frenkel origin.

The intermolecular interactions were quantified through TDDFT methods (Sec. S7), which estimate the strengths of the exciton coupling energy V and electron and hole transfer integrals t_e and t_h in dimer pairs extracted from R-Tc crystal structures.[15] The compar-

ison between coupling energies V (Tables S18-20) in various dimer pairs extracted from the crystal structures indicates that 'slip-stacked' derivatives (TES-, TMS-, tBu-Tc) have considerably more anisotropic exciton coupling V, with intermolecular interactions in the π-stacked or 'sandwiched' dimers (TES-α, tBu-β, and TMS-α) largely standing out among the rest. The dominant interacting dimer pairs in TBDMS-Tc (TBDMS-α and TBDMS-β) have a considerably lower V than those in the 'slip-stacked' derivatives, and the values of V among the three interacting dimer pairs in TBDMS-Tc are considerably more similar.

The more isotropic interactions could potentially play a role in entropy-driven ^{1}(TT) formation and dissociation,[80] lowering the activation barrier for separating the entangled triplet pairs, similarly to the charge carrier dynamics in organic semiconductors where more isotropic charge transfer integrals promote higher charge carrier mobility.[81] This is consistent with our observation of lower barriers ($E_{a,12}$ and $E_{a,24}$ in Table S10) in TBDMS-Tc than in TES-Tc. In previously studied TIPS-Tc, the calculation predicts a relatively isotropic distribution of low values of V (Table S21), which may promote ^{1}(TT) dissociation (thus partially balancing the higher energy barrier (2E(T1)-E(S1)) for SF) in TIPS-Tc as compared to the R-Tc derivatives under study.

The magnitudes of charge transfer integrals t_e and t_h relative to that of the exciton coupling energy V, were previously related to the propensity of the molecules to form excimer states.[15] In particular, functionalized anthradithiophene (diF R-ADT) crystals with packing motifs having pairs for which $|t_e|$ or $|t_h| \gg |V|$ were more prone to forming excimers as compared to those with $|t_e|, |t_h| \approx |V|$. The parameter values in Tables S18-S22 suggest that there would exist configurations conducive to excimer formation in all R-Tc derivatives (including TIPS-Tc). It is possible that defects in 'slip-stacked' derivatives skew the balance between V and t_e or t_h further, such that some of the low-energy Sx emission in these crystals is excimeric in origin, similar to that observed in TIPS-Tc.[82] On the other hand, it is possible that dimer pairs with $|t_e| \approx |t_h|$ (such as TBMDS-α and TES-γ) would support CT-mediated Dexter transfer[74] to aid in triplet pair separation.

4.3 Photochemistry depending on molecular packing

4.3.1 EPO formation

The main mechanism of degradation in air is considered to be formation of EPOs, which in tetracenes proceeds efficiently via the Type II mechanism due to the energy of triplet states T1 (Table S14) being higher than the 0.98 eV necessary to generate reactive singlet

oxygen ($^1O_2$) from the ground-state triplet oxygen ($^3O_2$).[16] This mechanism involves energy transfer from the T1 state of tetracene, typically formed via ISC in solution or SF in the solid state, to $^3O_2$ to generate $^1O_2$. Another mechanism of T1 generation is through oxygen sensitization, which utilizes the the energy difference E(S1)-E(T1)>0.98 eV (~1.2 eV in R-Tc, Tables S12 and S14) and which was also reported in acenes.[18] This process proceeds via singlet-triplet annihilation where the acene molecule in the excited singlet S1 state transfers the E(S1)-E(T1) excess energy to $^3O_2$, resulting in the acene molecule in the T1 state and the oxygen in the $^1O_2$ state ($S1 + {}^3O_2 \rightarrow T1 + {}^3O_2$). The singlet oxygen then may react with the Tc molecule in its ground state S0 or excited states S1 or T1 to form EPOs,[18,44] which is the mechanism responsible for EPO formation in dilute TIPS-Tc solutions where SF is inefficient.[18] Once the reactive oxygen is generated, the photo-oxidation reaction could proceed with the TIPS-Tc molecule in any state, but only TIPS-Tc molecules in their T1 states had considerable reaction rates, whereas EPO formation from S1 or S0 states was negligible.[18] Based on these considerations, higher population of free triplets T1 is expected to promote degradation via EPO formation, but the reaction is still possible for molecules not participating in SF.

Our experiments exploring EPO formation in R-Tc crystals side by side with the photo-physical studies enable relating photophysical and photochemical properties which we probed via time evolution of optical absorption and PL properties during the photodegradation-inducing illumination. The optical absorption probes an entire molecular population, whereas PL reports on the emissive populations (<1% of the total population at room temperature) and kinetically connected dark populations. The photodegradation probed both through the optical absorption and PL was considerably slower in TBDMS-Tc crystals as compared to TES-Tc (Figs. 10-11). This is interesting because our model predicts only a slightly lower generation rate for the free triplets T1 in TBDMS-Tc as compared to TES-Tc at room temperature (Fig. 7b), which would be expected to promote both the reactive oxygen generation and subsequent reaction.

A further insight is obtained from comparison between photodegradation of the molecular populations responsible for the 1a and 1b features in the absorption spectra of TES-Tc and TBDMS-Tc crystals (Fig. 10a,c). While in TBDMS-Tc, these decayed similarly and uniformly under continuous illumination, significant differences were observed in TES-Tc where the 1a feature clearly degraded considerably faster than the 1b. In 'slip-stacked' crystalline acenes, the lowest-energy absorption (such as S1a in TES-Tc) was theoretically predicted to have a transition dipole moment along the $\pi - \pi$ stacking direction.[39] Therefore,

the rapid degradation of 1a suggests that ^{1}(TT) states form and dissociate into free triplets T1 predominantly along the 'slip-stack' direction, which promotes degradation of the molecules forming such 'slip-stacks'. The 1b feature in TES-Tc initially has a slow degradation rate, matching that in TBDMS-Tc, which then accelerates. This may suggest that the 'slip-stacked' molecular arrangements disrupted by initially degraded molecules open up efficient pathways for oxygen diffusion, as was observed in rubrene crystals.[22] Such acceleration is absent in TBDMS-Tc which is the key to its enhanced stability in air as compared to TES-Tc.

The PL-based degradation data provides further clues to the molecular populations affected by degradation. The fast destruction of the 1a absorption feature in TES-Tc coincides with a rapid increase in PL from S1 and S1agg states as the molecules in configurations conducive to SF, forming ^{1}(TT) and T1 states are destroyed. High B-fields slow down the T1 and reactive oxygen production, which delays the R-Tc degradation in air. Additional B-field dependence may arise from the spin-dependent kinetics of biradical stepwise mechanism of the EPO formation itself,[69] as observed, for example, in the reverse reaction to the EPO formation, the EPO thermolysis, of acenes where high B-fields impede the release of the singlet oxygen.[83] The destruction of molecules capable of SF prolongs the lifetime of the surviving molecules in singlet states S1, S1agg, and Sx. This makes them more vulnerable for chemical reactions via mechanisms of reactive oxygen generation from singlet states (such as that discussed above[18]) and/or the Type II mechanism involving triplet states produced via ISC, ultimately leading to the degradation of most of the emissive molecules in R-Tc crystals and films in air (Fig. 11).

4.3.2 Photodimerization

In contrast to EPO formation where morphology plays a secondary to role to the excited state dynamics, both the photophysics and morphology are important for photodimerization.[69] Previous studies established that the 'butterfly' photodimer formation in unsubstituted acenes occurs from singlet states, possibly with an excimer as a precursor.[84,85]

The crystals of 'slip-stacked' TES-, TMS-, and tBu-Tc derivatives were more susceptible to photodimerization than 'gamma'-packed TBDMS-Tc.[23] In TBDMS-Tc, most molecules do not meet the positional requirements for photodimerization and are relatively stable. This is in contrast to TES-Tc, in which the molecules that form ^{1}(TT) and Sx states are most susceptible to photodimerization, while the molecular populations responsible for the S1 and S1agg emission are stable in oxygen-free environments. Similar considerations are applicable to the two other 'slip-stacked', TMS-and tBu-Tc, crystals and amorphous TES-Tc films.

It is interesting that the effect of high B-field on photodimerization of TES-Tc, although weaker, is qualitatively similar to that on the EPO formation: high B-field slows down the photodegradation dynamics (Figs. 11-12). This indicates that ^{1}(TT) and T1 states may play a role in both mechanisms. For example, high B-fields could affect the unlikely but possible formation of excimers as a product of triplet-triplet annihilation[86] that serve as a precursor to photodimerization (e.g. T1+T1 → ^{1}(TT) → excimer → photodimer) and, additionally, modify the potential energy surfaces that modulate the photodimerization reaction barrier itself.[87] The overall effect is that the photodimerization rate is slower, but the photodimerization-affected population is higher at 6 T as compared to 0 T. Formation of such excimer states is less supported by the TBDMS-Tc crystal structure, enhancing its stability.

5 Conclusions

We applied a combination of spectroscopy techniques, kinetic modeling, and TDDFT analysis to study photophysics and photochemistry of R-Tc crystals and films with different molecular packing. In both the 'gamma'-packed TBDMS-Tc and 'slip-stacked' TES-Tc crystals, temperature-independent and thermally activated pathways of formation and dissociation of ^{1}(TT) states were observed, with free triplet yields of 191±2% (58±6%) and 181±4% (29±4%) in TES-Tc and TBDMS-Tc, respectively, at 300 K (1.6 K) predicted by the kinetic model. We established that the TES-Tc derivative is superior to TBDMS-Tc in terms of forming ^{1}(TT) states and dissociating ^{1}(TT) states into free triplets at all temperatures, but especially below 150 K. All three 'slip-stacked' R-Tc derivatives (TES-Tc, TMS-Tc, and tBu-Tc) exhibited formation of dimer-like defects responsible for low-energy emission (Sx) in films and serving as exciton traps in crystals. Such emission was absent in TBDMS-Tc; instead, a J-aggregate-like emission (S1agg), likely due to a relaxed S1 exciton, dominated the emissive properties of TBDMS-Tc crystals. When S1agg and Sx are populated from S1, their emission is kinetically connected to the ^{1}(TT) formation and dissociation, which manifests in the temperature and B-field dependence of PL from these states such that the PL is higher at lower temperatures (by two orders of magnitude at 1.6 K than at 300 K) and at strong B-fields (by ~20-50% at 7 T, depending on the derivative). Even at 1.6 K, positive MFEs are observed in R-Tc crystals due to the presence of a non-thermally-activated SF pathway.

The 'slip-stacked' TES-Tc derivative was found to be considerably more prone to pho-

todegradation both via the EPO formation in air and the photodimerization in vacuum as compared to the 'gamma'-packed TBDMS-Tc. In TES-Tc in air, the molecules in dark ^{1}(TT) and T1 states degraded first, followed by the emissive molecules in singlet states. In vacuum, only the TES-Tc molecules in dark states and in emissive low-energy Sx states photodimerized, dramatically increasing the PL emission from the higher-energy S1 and S1agg states of molecules in configurations resistant to photodimerization. Both the EPO formation and photodimerization in TES-Tc were slower under high B-fields, highlighting the role of the triplet states in the degradation dynamics via both mechanisms.

At room temperature, TBDMS-Tc and TES-Tc structures support similarly high SF yields, but TBDMS-Tc is superior in terms of photostability both with respect to EPO formation in air and photodimerization in vacuum. Therefore, it is possible to achieve high photostability simultaneously with efficient SF by selecting an appropriate packing motif. While the 'slip-stack' motif of TES-Tc promotes efficient SF at lower temperatures, the 'gamma' motif of TBDMS-Tc offers both efficient SF and high photostability for optoelectronic devices operating under ambient conditions.

Supplementary Material

See Supplementary Material for additional crystal structure and spectral data, details on fits and fit parameters, kinetic modeling, and DFT procedures and results.

Acknowledgements

We thank Dr. S. Parkin for single-crystal XRD structure determination. This work was supported by the National Science Foundation (NSF) (CHE-1956431). The synthesis of organic semiconductors was supported by the NSF DMR (DMREF-1627428). Sample fabrication and characterization was partially performed in NSF-funded user facilities via NNCI:NNI EECS-2025489 and MRI DMR-1920368 grants.

Author Declarations

Conflicts of Interest

The authors have no conflicts to disclose

Author Contributions

Winston T. Goldthwaite: Investigation, Methodology, Formal analysis, Writing - original draft. **Evan Lambertson**: Formal analysis, Writing - original draft. **Madalyn Gragg**: Investigation, Writing - review and editing. **Dean Windemuller**: Resources, Writing - review and editing. **John E. Anthony**: Writing - review and editing, Resources. **Tim Zuehlsdorff** : Writing - review and editing. **Oksana Ostroverkhova**: Conceptualization, Supervision, Project Administration, Funding Acquisition, Writing - original draft.

Data Availability

The data that support the findings of this study are available from the corresponding author upon reasonable request.

References

[1] Alexander J. Baldacchino, Miles I. Collins, Michael P. Nielsen, Timothy W. Schmidt, Dane R. McCamey, and Murad J. Y. Tayebjee. Singlet fission photovoltaics: Progress and promising pathways. *Chemical Physics Reviews*, 3(2):021304, 2022.

[2] Benjamin Daiber, Koen Van Den Hoven, Moritz H. Futscher, and Bruno Ehrler. Realistic Efficiency Limits for Singlet-Fission Silicon Solar Cells. *ACS Energy Letters*, 6(8):2800–2808, 2021.

[3] Andrew J. Musser and Jenny Clark. Triplet-Pair States in Organic Semiconductors. *Annual Review of Physical Chemistry*, 70:323–351, 2019.

[4] Dezheng Sun, Gang Hua Deng, Bolei Xu, Enshi Xu, Xia Li, Yajing Wu, Yuqin Qian, Yu Zhong, Colin Nuckolls, Avetik R. Harutyunyan, Hai Lung Dai, Gugang Chen, Hanning Chen, and Yi Rao. Anisotropic Singlet Fission in Single Crystalline Hexacene. *iScience*, 19:1079–1089, 2019.

[5] Juno Kim, David C Bain, Vivian Ding, Kanad Majumder, Dean Windemuller, Jiaqi Feng, Jishan Wu, Satish Patil, John Anthony, Woojae Kim, and Andrew J Musser. Coherent photoexcitation of entangled triplet pair states. *Nature Chemistry*, 2024.

[6] Yan Wan, Gary P. Wiederrecht, Richard D. Schaller, Justin C. Johnson, and Libai Huang. Transport of Spin-Entangled Triplet Excitons Generated by Singlet Fission. *Journal of Physical Chemistry Letters*, 9(23):6731–6738, 2018.

[7] Markus Einzinger, Tony Wu, Julia F. Kompalla, Hannah L. Smith, Collin F. Perkinson, Lea Nienhaus, Sarah Wieghold, Daniel N. Congreve, Antoine Kahn, Moungi G. Bawendi, and Marc A. Baldo. Sensitization of silicon by singlet exciton fission in tetracene. *Nature*, 571(7763):90–94, 2019.

[8] Benjamin Daiber, Sidharam P. Pujari, Steven Verboom, Stefan L. Luxembourg, Stefan W. Tabernig, Moritz H. Futscher, Jumin Lee, Han Zuilhof, and Bruno Ehrler. A method to detect triplet exciton transfer from singlet fission materials into silicon solar cells: Comparing different surface treatments. *Journal of Chemical Physics*, 152(11), 2020.

[9] S. L. Bayliss, L. R. Weiss, A. Mitioglu, K. Galkowski, Z. Yang, K. Yunusova, A. Surrente, K. J. Thorley, J. Behrends, R. Bittl, J. E. Anthony, A. Rao, R. H. Friend, P. Plochocka, P. C.M. Christianen, N. C. Greenham, and A. D. Chepelianskii. Site-selective measurement of coupled spin pairs in an organic semiconductor. *Proceedings of the National Academy of Sciences of the United States of America*, 115(20):5077–5082, 2018.

[10] Yuqing Huang, Irina A. Buyanova, Chanakarn Phansa, Maria E. Sandoval-Salinas, David Casanova, William K. Myers, Neil C. Greenham, Akshay Rao, Weimin M. Chen, and Yuttapoom Puttisong. Competition between triplet pair formation and excimer-like recombination controls singlet fission yield. *Cell Reports Physical Science*, 2(2):100339, 2021.

[11] Cameron B. Dover, Joseph K. Gallaher, Laszlo Frazer, Patrick C. Tapping, Anthony J. Petty, Maxwell J. Crossley, John E. Anthony, Tak W. Kee, and Timothy W. Schmidt. Endothermic singlet fission is hindered by excimer formation. *Nature Chemistry*, 10(3):305–310, 2018.

[12] Hannah L. Stern, Alexandre Cheminal, Shane R. Yost, Katharina Broch, Sam L. Bayliss, Kai Chen, Maxim Tabachnyk, Karl Thorley, Neil Greenham, Justin M. Hodgkiss, John Anthony, Martin Head-Gordon, Andrew J. Musser, Akshay Rao, and Richard H. Friend. Vibronically coherent ultrafast triplet-pair formation and subsequent thermally activated dissociation control efficient endothermic singlet fission. *Nature Chemistry*, 9(12):1205–1212, 2017.

[13] Arya Thampi, Hannah L. Stern, Alexandre Cheminal, Murad J.Y. Tayebjee, Anthony J. Petty, John E. Anthony, and Akshay Rao. Elucidation of Excitation Energy Dependent Correlated Triplet Pair Formation Pathways in an Endothermic Singlet Fission System. *Journal of the American Chemical Society*, 140(13):4613–4622, 2018.

[14] Andrew D. Platt, Jonathan Day, Sankar Subramanian, John E. Anthony, and Oksana Ostroverkhova. Optical, fluorescent, and (photo)conductive properties of high-performance functionalized pentacene and anthradithiophene derivatives. *Journal of Physical Chemistry C*, 113(31):14006–14014, 2009.

[15] J. D.B. Van Schenck, G. Mayonado, J. E. Anthony, M. W. Graham, and O. Ostroverkhova. Molecular packing-dependent exciton dynamics in functionalized anthradithiophene derivatives: From solutions to crystals. *Journal of Chemical Physics*, 153(16), 2020.

[16] Werner Fudickar and Torsten Linker. Why Triple Bonds Protect Acenes from Oxidation and Decomposition. *Journal of the American Chemical Society*, 134:15071–15082, 2012.

[17] Laila Abu-Sen, John J. Morrison, Andrew B. Horn, and Stephen G. Yeates. Concentration- and solvent-dependent photochemical instability of 6,13-bis(triisopropysilylethynyl)pentacene. *Advanced Optical Materials*, 2(7):636–640, 2014.

[18] Alexandra N Stuart, Tak W Kee, and David M Huang. Role of Singlet and Triplet Excited States in the Oxygen-Mediated Photophysics and Photodegradation of Polyacenes. *Journal of the Americal Chemical Society*, 146:2174–2186, 2024.

[19] Ashok Maliakal, Krishnan Raghavachari, Howard Katz, Edwin Chandross, and Theo Siegrist. Photochemical Stability of Pentacene and a Substituted Pentacene in Solution and in Thin Films. *Chemistry of Materials*, 16(24):4980–4986, 2004.

[20] Richard Puro, Jonathan D.B. Van Schenck, Reid Center, Emma K. Holland, John E. Anthony, and Oksana Ostroverkhova. Exciton Polariton-Enhanced Photodimerization of Functionalized Tetracene. *Journal of Physical Chemistry C*, 125(49):27072–27083, 2021.

[21] W.E.B. Shepherd, R. Grollman, a. Robertson, K. Paudel, R. Hallani, M.a. Loth, J.E. Anthony, and O. Ostroverkhova. Single-molecule imaging of organic semiconductors:

Toward nanoscale insights into photophysics and molecular packing. *Chemical Physics Letters*, 629:29–35, 2015.

[22] Hikmet Najafov, Daniel Mastrogiovanni, Eric Garfunkel, Leonard C. Feldman, and Vitaly Podzorov. Photon-assisted oxygen diffusion and oxygen-related traps in organic semiconductors. *Advanced Materials*, 23(8):981–985, 2011.

[23] Winston T Goldthwaite, Michael O Chase, Madalyn R Gragg, Roshell Lamug, Dean Windemuller, Sean Parkin, John E Anthony, and Oksana Ostroverkhova. Elucidating photophysics-photochemistry relationship in singlet fission materials. *MRS Advances*, 9:707—-714, 2024.

[24] Paolo Coppo and Stephen G. Yeates. Shining light on a pentacene derivative: The role of photoinduced cycloadditions. *Advanced Materials*, 17(24):3001–3005, 2005.

[25] Tianying Wang, Heyuan Liu, Xianyuan Wang, Linglong Tang, Jun Zhou, Xiaojuan Song, Liping Lv, Wenmiao Chen, Yanli Chen, and Xiyou Li. Employing Singlet Fission into Boosting the Generation of Singlet Oxygen and Superoxide Radicals for Photooxidation Reactions. *ACS Catalysis*, 13(21):13902–13911, 2023.

[26] Y. Liu, J. Li, S. Gong, Y. Yu, Z. Zhu, C. Ji, Z. Zhao, X. Chen, G. Feng, and B. Tang. Achieving beyond 100% Triplet State Generation with Singlet Fission Strategy for High-Performance Photosensitizer Design. *ACS Materials Letters*, 6:896–907, 2024.

[27] Connor J. Easley, Fei Tong, Xinning Dong, Rabih O. Al-Kaysi, and Christopher J. Bardeen. Using light intensity to control reaction kinetics and reversibility in photomechanical crystals. *Chemical Science*, 11(36):9852–9862, 2020.

[28] Leigh Loots and Leonard J Barbour. A rudimentary method for classification of $\pi \ldots \pi$ packing motifs for aromatic molecules. *The Importance of Pi-Interactions in Crystal Engineering: Frontiers in Crystal Engineering*, pages 109–124, 2012.

[29] Jonathan D.B. Van Schenck, Winston T. Goldthwaite, Richard Puro, John E. Anthony, and Oksana Ostroverkhova. Exciton Polaritons Reveal "Hidden" Populations in Functionalized Pentacene Films. *Journal of Physical Chemistry C*, 125(49):27381–27393, 2021.

[30] M. Frisch, G. Trucks, H. Schlegel, G. Scuseria, M. Robb, M. Cheeseman, G. Scalmani, V. Barone, G. Petersson, and H. Nakatsuii. Gaussian 16, 2016.

[31] T. Yanai, D. Tew, and N. Handy. A new hybrid exchange–correlation functional using the Coulomb-attenuating method (CAM-B3LYP). *Chemical Physics Letters*, 393:51–57, 2004.

[32] Jr. Dunning, Thom H. Gaussian basis sets for use in correlated molecular calculations. I. The atoms boron through neon and hydrogen. *The Journal of Chemical Physics*, 90(2):1007–1023, 01 1989.

[33] M. J. Kendrick, a. Neunzert, M. M. Payne, B. Purushothaman, B. D. Rose, J. E. Anthony, M. M. Haley, and O. Ostroverkhova. Formation of the donor-acceptor charge-transfer exciton and its contribution to charge photogeneration and recombination in small-molecule bulk heterojunctions. *Journal of Physical Chemistry C*, 116(34):18108–18116, 2012.

[34] Alexandra N. Stuart, Patrick C. Tapping, Tak W. Kee, and David M. Huang. Pitfalls of quantifying intersystem crossing rates in singlet-fission chromophore solutions. *Journal of Chemical Physics*, 157(8), 2022.

[35] Z. Birech, M. Schwoerer, T. Schmeiler, J. Pflaum, and H. Schwoerer. Ultrafast dynamics of excitons in tetracene single crystals. *Journal of Chemical Physics*, 140:114501, 2014.

[36] N J Hestand, H Yamagata, Bolei Xu, Dezheng Sun, Yu Zhong, Avetik R Harutyunyan, Gugang Chen, Hai-lung Dai, Yi Rao, and F C Spano. Polarized Absorption in Crystalline Pentacene : Theory vs Experiment. *Journal of Physical Chemistry C*, 119:22137–22147, 2015.

[37] Caterina Cocchi, Tobias Breuer, Gregor Witte, and C. Draxl. Polarized absorbance and Davydov splitting in bulk and thin-film pentacene polymorphs. *Physical Chemistry Chemical Physics*, 20:29724, 2018.

[38] Lukas Graf, Fupin Liu, Marco Naumann, Friedrich Roth, Bipasha Debnath, Bernd Büchner, Yulia Krupskaya, Alexey A. Popov, and Martin Knupfer. Optical anisotropy and momentum-dependent excitons in dibenzopentacene single crystals. *ACS Omega*, 7(24):21183–21191, 2022.

[39] Ling Yi Huang, Qianxiang Ai, and Chad Risko. The role of crystal packing on the optical response of trialkyltetrelethynyl acenes. *Journal of Chemical Physics*, 157(8), 2022.

[40] R Eric Mcanally, Jon A Bender, Laura Estergreen, Ralf Haiges, Stephen E Bradforth, Jahan M Dawlaty, Sean T Roberts, and Aaron S Rury. Defects Cause Subgap Luminescence from a Crystalline Tetracene. *Journal of Physical Chemistry Letters*, 8:5993–6001, 2017.

[41] Marco Rosenkranz, Lukas Graf, Bernd Büchner, Martin Knupfer, and Alexey A Popov. Photoluminescence spectroscopy of dibenzopentacene single-crystals: multiple emissive states across temperature, time, and magnetic field in a pursuit of exothermic singlet fission. *Journal of Materials Chemistry C*, 11(37):12714–12729, 2023.

[42] Andrew C. Jones, Nicholas M. Kearns, Jia Jung Ho, Jessica T. Flach, and Martin T. Zanni. Impact of non-equilibrium molecular packings on singlet fission in microcrystals observed using 2D white-light microscopy. *Nature Chemistry*, 12(1):40–47, 2020.

[43] Tai Sang Ahn, Astrid M. Müller, Rabih O. Al-Kaysi, Frank C. Spano, Joseph E. Norton, David Beljonne, Jean Luc Bŕdas, and Christopher J. Bardeen. Experimental and theoretical study of temperature dependent exciton delocalization and relaxation in anthracene thin films. *Journal of Chemical Physics*, 128(5):054505, 2008.

[44] Reza Dabestani, Mark Nelson, and Michael E. Sigman. Photochemistry of tetracene adsorbed on dry silica: Products and mechanism. *Photochemistry and Photobiology*, 64(1):80–86, 1996.

[45] M. Iannone and G. Scott. Low temperature emission spectra of trapped tetracene pairs from ditetracene. *Chemical Physics Letters*, 171:569, 1990.

[46] G Fournie, F Dupuy, M Martinaud, G Nouchi, and JM Turlet. Auto-association of tetracene in solution. *Chemical Physics Letters*, 16(2):332–335, 1972.

[47] Javier Catalán. On dimers and complexes of tetracene and the kasha's molecular excitonic model. *Journal of Physical Organic Chemistry*, 27(5):456–462, 2014.

[48] Sang Hyun Lim, Thomas G. Bjorklund, Frank C. Spano, and Christopher J. Bardeen. Exciton Delocalization and Superradiance in Tetracene Thin Films and Nanoaggregates. *Physical Review Letters*, 92(10):107402–1, 2004.

[49] H. Yamagata, J. Norton, E. Hontz, Y. Olivier, D. Beljonne, J. L. Brédas, R. J. Silbey, and F. C. Spano. The nature of singlet excitons in oligoacene molecular crystals. *Journal of Chemical Physics*, 134(20):204703, 2011.

[50] N. Geacintov, M. Pope, and F. Vogel. Effect of magnetic field on the fluorescence of tetracene crystals: Exciton fission. *Phys. Rev. Lett.*, 22:593–596, Mar 1969.

[51] Chad D. Cruz, Eric L. Chronister, and Christopher J. Bardeen. Using temperature dependent fluorescence to evaluate singlet fission pathways in tetracene single crystals. *Journal of Chemical Physics*, 153(23), 2020.

[52] Geoffrey B. Piland and Christopher J. Bardeen. How Morphology Affects Singlet Fission in Crystalline Tetracene. *The Journal of Physical Chemistry Letters*, 6:1841–1846, 2015.

[53] S. Arnold, R. R. Alfano, M. Pope, W. Yu, P. Ho, R. Selsby, J. Tharrats, and C. E. Swenberg. Triplet exciton caging in two dimensions. *The Journal of Chemical Physics*, 64(12):5104–5114, 06 1976.

[54] Gina Mayonado, Kyle T. Vogt, Jonathan D.B. Van Schenck, Liangdong Zhu, Garrett Fregoso, John Anthony, Oksana Ostroverkhova, and Matt W. Graham. High-Symmetry Anthradithiophene Molecular Packing Motifs Promote Thermally Activated Singlet Fission. *Journal of Physical Chemistry C*, 126(9):4433–4445, 2022.

[55] Nicholas J. Thompson, Eric Hontz, Wendi Chang, Troy Van Voorhis, and Marc Baldo. Magnetic feld dependence of singlet fssion in solutions of diphenyl tetracene. *Philosophical Transactions of the Royal Society A: Mathematical, Physical and Engineering Sciences*, 373(2044), 2015.

[56] Geoffrey B. Piland, Jonathan J. Burdett, Dharmalingam Kurunthu, and Christopher J. Bardeen. Magnetic field effects on singlet fission and fluorescence decay dynamics in amorphous rubrene. *Journal of Physical Chemistry C*, 117(3):1224–1236, 2013.

[57] Patrick C. Tapping and David M. Huang. Comment on "Magnetic field effects on singlet fission and fluorescence decay dynamics in amorphous rubrene". *Journal of Physical Chemistry C*, 120(43):25151–25157, 2016.

[58] David G. Bossanyi, Yoichi Sasaki, Shuanqing Wang, Dimitri Chekulaev, Nobuo Kimizuka, Nobuhiro Yanai, and Jenny Clark. In optimized rubrene-based nanoparticle blends for photon upconversion, singlet energy collection outcompetes triplet-pair separation, not singlet fission. *Journal of Materials Chemistry C*, 10(12):4684–4696, 2021.

[59] Kei Ishikawa, Tomoaki Yago, and Masanobu Wakasa. Exploring the Structure of an Exchange-Coupled Triplet Pair Generated by Singlet Fission in Crystalline Diphenylhexatriene: Anisotropic Magnetic Field Effects on Fluorescence in High Fields. *Journal of Physical Chemistry C*, 122(39):22264–22272, 2018.

[60] Masanobu Wakasa, Tomoaki Yago, Yoriko Sonoda, and Ryuzi Katoh. Structure and dynamics of triplet-exciton pairs generated from singlet fission studied via magnetic field effects. *Communications Chemistry*, 1(1):1–6, 2018.

[61] Hyuk Jae Jang. The Effect of Magnetic Fields on Singlet Fission in Organic Semiconductors: its Understanding and Applications. *ChemPhotoChem*, 4(10):5135–5146, 2020.

[62] Christopher J Bardeen. The structure and dynamics of molecular excitons. *Annual review of physical chemistry*, 65:127–48, 2014.

[63] Tomoaki Yago, Kei Ishikawa, Ryuzi Katoh, and Masanobu Wakasa. Magnetic field effects on triplet pair generated by singlet fission in an organic crystal: Application of radical pair model to triplet pair. *The Journal of Physical Chemistry C*, 120(49):27858–27870, 2016.

[64] Vadim V. Tarasov, George E. Zoriniants, Anatoli I. Shushin, and Michael M. Triebel. The role of spin-lattice relaxation in magnetic field effects on the luminescence of amorphous and polycrystalline rubrene films. *Chemical Physics Letters*, 267(1):58–64, 1997.

[65] Kyle T. Munson, Jianing Gan, Christopher Grieco, Grayson S. Doucette, John E. Anthony, and John B. Asbury. Ultrafast Triplet Pair Separation and Triplet Trapping following Singlet Fission in Amorphous Pentacene Films. *Journal of Physical Chemistry C*, 124(43):23567–23578, 2020.

[66] Jens Reichwagen, Henning Hopf, Del Guerzo, Jean-pierre Desvergne, and Henri Bouas-laurent. Photodimers of a Soluble Tetracene Derivative . Excimer Fluorescence from the Head-to-Head Isomer. *Organic Letters*, 6:1899–1902, 2004.

[67] Shaoqiang Dong, Albert Ong, and Chunyan Chi. Photochemistry of various acene based molecules. *Journal of Photochemistry & Photobiology C*, 38:27–46, 2019.

[68] Pei Cheng and Xiaowei Zhan. Stability of organic solar cells: challenges and strategies. *Chem. Soc. Rev.*, 45:2544–2582, 2016.

[69] Sanjio S. Zade and Michael Bendikov. Reactivity of acenes: Mechanisms and dependence on acene length. *Journal of Physical Organic Chemistry*, 25(6):452–461, 2012.

[70] Miles I. Collins, Francesco Campaioli, Murad J.Y. Tayebjee, Jared H. Cole, and Dane R. McCamey. Quintet formation, exchange fluctuations, and the role of stochastic resonance in singlet fission. *Communications Physics*, 6(1):11–13, 2023.

[71] Guodong Wang, Chunfeng Zhang, Zhixing Liu, Rui Wang, Haibo Ma, Xiaoyong Wang, and Min Xiao. Singlet fission dynamics in tetracene single crystals probed by polarization-dependent two-dimensional electronic spectroscopy. *Journal of Physical Chemistry A*, 124(50):10447–10456, 2020.

[72] Kiyoshi Miyata, Yuki Kurashige, Kazuya Watanabe, Toshiki Sugimoto, Shota Takahashi, Shunsuke Tanaka, Jun Takeya, Takeshi Yanai, and Yoshiyasu Matsumoto. symmetry breaking. *Nature Chemistry*, 9(10):983–989, 2017.

[73] Tia S. Lee, YunHui L. Lin, Hwon Kim, Barry P. Rand, and Gregory D. Scholes. Two temperature regimes of triplet transfer in the dissociation of the correlated triplet pair after singlet fission. *Canadian Journal of Chemistry*, 97(6):465–473, 2019.

[74] Jens Wehner and Björn Baumeier. Intermolecular singlet and triplet exciton transfer integrals from many-body green's functions theory. *Journal of Chemical Theory and Computation*, 13(4):1584–1594, 2017. PMID: 28234472.

[75] Sam L. Bayliss, Felix Kraffert, Rui Wang, Chunfeng Zhang, Robert Bittl, and Jan Behrends. Tuning Spin Dynamics in Crystalline Tetracene. *Journal of Physical Chemistry Letters*, 10(8):1908–1913, 2019.

[76] V. Coropceanu, J. Cornil, D. a. Da Silva Filho, Y. Olivier, R. J. Silbey, and J.-L. Bredas. Charge transport in organic semiconductors. *Chemical Reviews*, 107:926–952, 2007.

[77] R. J. Charlton, R. M. Fogarty, S. Bogatko, T. J. Zuehlsdorff, N. D. M. Hine, M. Heeney, A. P. Horsfield, and P. D. Haynes. Implicit and explicit host effects on excitons in pentacene derivatives. *The Journal of Chemical Physics*, 148(10):104108, 03 2018.

[78] D. Beljonne, H. Yamagata, J. L. Brédas, F. C. Spano, and Y. Olivier. Charge-transfer excitations steer the Davydov splitting and mediate singlet exciton fission in pentacene. *Physical Review Letters*, 110(22):226402, 2013.

[79] Alexander Neef, Samuel Beaulieu, Sebastian Hammer, Shuo Dong, Julian Maklar, Tommaso Pincelli, R. Patrick Xian, Martin Wolf, Laurenz Rettig, Jens Pflaum, and Ralph Ernstorfer. Orbital-resolved observation of singlet fission. *Nature*, 616(7956):275–279, 2023.

[80] Anatoly B. Kolomeisky, Xintian Feng, and Anna I. Krylov. A simple kinetic model for singlet fission: A role of electronic and entropic contributions to macroscopic rates. *Journal of Physical Chemistry C*, 118(10):5188–5195, 2014.

[81] O. Ostroverkhova. Organic optoelectronic materials : mechanisms and applications. *Chemical Reviews*, 116:13279–13412, 2016.

[82] Cameron B Dover, Joseph K Gallaher, Laszlo Frazer, Patrick C Tapping, Anthony J Petty Ii, Maxwell J Crossley, John E Anthony, Tak W Kee, and Timothy W Schmidt. Endothermic singlet fission is hindered by excimer formation. *Nature Chemistry*, 10:305, 2018.

[83] Nicholas J Turro and Ming-Fea Chow. Magnetic field effects on the thermolysis of endoperoxides of aromatic compounds. correlations with singlet oxygen yield and activation entropies. *Journal of the American Chemical Society*, 101(13):3701–3703, 1979.

[84] James L. Charlton, Reza Dabestani, and Jack Saltiel. Role of Triplet-Triplet Annihilation in Anthracene Dimerization1a. *Journal of the American Chemical Society*, 105(11):3473–3476, 1983.

[85] Fei Tong, Mervin P. Hanson, and Christopher J. Bardeen. Analysis of reaction kinetics in the photomechanical molecular crystal 9-methylanthracene using an extended Finke–Watzky model. *Physical Chemistry Chemical Physics*, 18(46):31936–31945, 2016.

[86] Chen Ye, Victor Gray, Jerker Mårtensson, and Karl Börjesson. Annihilation Versus Excimer Formation by the Triplet Pair in Triplet-Triplet Annihilation Photon Upconversion. *Journal of the American Chemical Society*, 141(24):9578–9584, 2019.

[87] ME Frink, DK Geiger, and GJ Ferraudi. Excimer formation from triplet-triplet annihilation reactions of the lowest-lying triplet excited state in aluminum (iii), silicon (iv), and metal-free phthalocyanines: medium and magnetic field effects on the rate of reaction. *The Journal of Physical Chemistry*, 90(9):1924–1927, 1986.